ACS APPLIED MATERIALS & INTERFACES

www.acsami.org

Research Article

Multimodal Locomotion of Amphibious Soft Microrobots for Multi-Environment Exploration

Chenglin Li, Jing Li, and Xin Yi*

Cite This: ACS Appl. Mater. Interfaces 2025, 17, 47456−47465

Read Online

ACCESS | Metrics & More | Article Recommendations | Supporting Information

ABSTRACT: Amphibious robots have immense potential for exploration in complex environments, but rigid and intricate structures limit adaptability and may cause mechanical disruption or ecological damage. This study presents a novel amphibious soft microrobot capable of seamlessly transitioning between land and water locomotion. We leverage the high power density and reversible actuation of 4D-printed liquid crystal elastomers (LCEs) combined with flexible heating circuits to fabricate LCE amphibious actuators. These actuators enable large deformation, providing sufficient power for locomotion on both land and water. To enable controllable swimming, we design a buoyancy-regulating module inspired by the swim bladder of fish. This module consists of a liquid-filled elastomer integrated with flexible heating circuits, allowing dynamic tuning of the robot's buoyancy for stable underwater propulsion. We systematically characterize the robot's amphibious and multidirectional locomotion, demonstrating its ability to hover at different depths, swim in multiple directions, cross obstacles, and navigate narrow gaps. The proposed design offers a simple yet highly deformable structure, enabling seamless transitions between crawling and swimming, paving the way for advanced applications in environmental monitoring and exploration.

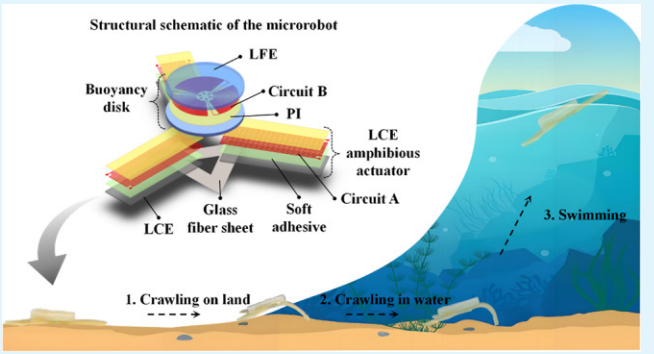

KEYWORDS: *amphibious microrobots, locomotion mechanisms, environmental adaptability, liquid-filled elastomers, soft actuators*

INTRODUCTION

Amphibious robots have attracted significant research interest in recent decades due to their ability to perform multimodal exploration and environmental monitoring across both land and water.[1−5] Most existing designs rely on multiple, discrete propulsion mechanisms—such as wheels, legs, paddles, or fins—integrated within modular or transformable architectures to adapt to different environments. While this approach enhances functional versatility, it also introduces significant structural complexity and hinders scalability. For example, leg−flipper transformation systems typically require dedicated actuators and mechanical linkages to switch between modes, whereas coaxial wheel−propeller−fin modules often depend on separate motors and gear sets to transition between land and water locomotion.[6−9] These systems commonly incorporate rigid components and solid external shells, which increase their overall size and weight (e.g., >15 cm, >20 g),[10−13] limit their maneuverability in confined or sensitive environments, and elevate the risk of mechanical failure at structural interfaces. Furthermore, the energy demands and synchronization requirements associated with mode switching reduce their robustness in dynamic or unstructured terrains.

To address these challenges, we propose an amphibious soft microrobot with notable deformability, reliable environmental adaptability, and ease of fabrication with a simplified structural design. This platform is specifically engineered to transition seamlessly between land locomotion and underwater swimming, thereby mitigating the drawbacks of existing systems.

Currently, smart materials primarily include hydrogels, shape memory alloys and polymers, liquid crystal elastomers (LCEs), dielectric elastomers, and magnetic composites.[14−19] Among these, LCEs are particularly attractive due to their excellent reversible deformability, programmability, processability, and responsiveness to various external stimuli. Central to our approach is the use of LCEs as the soft actuation medium. LCEs have emerged as promising materials for constructing soft robots,[20−22] wearable devices,[23−26] artificial muscles,[27,28] and biomimetic system.[29−31] Their actuation is driven by the realignment of liquid crystal mesogens during the phase transition from nematic to isotropic states, which enables large reversible deformation (approximately 40%) coupled with high power density. Prior studies have demonstrated various actuation methods for LCEs—ranging from heat plates[32,33]

Received: April 29, 2025
Revised: July 28, 2025
Accepted: July 30, 2025
Published: August 6, 2025

https://doi.org/10.1021/acsami.5c08610
ACS Appl. Mater. Interfaces 2025, 17, 47456−47465

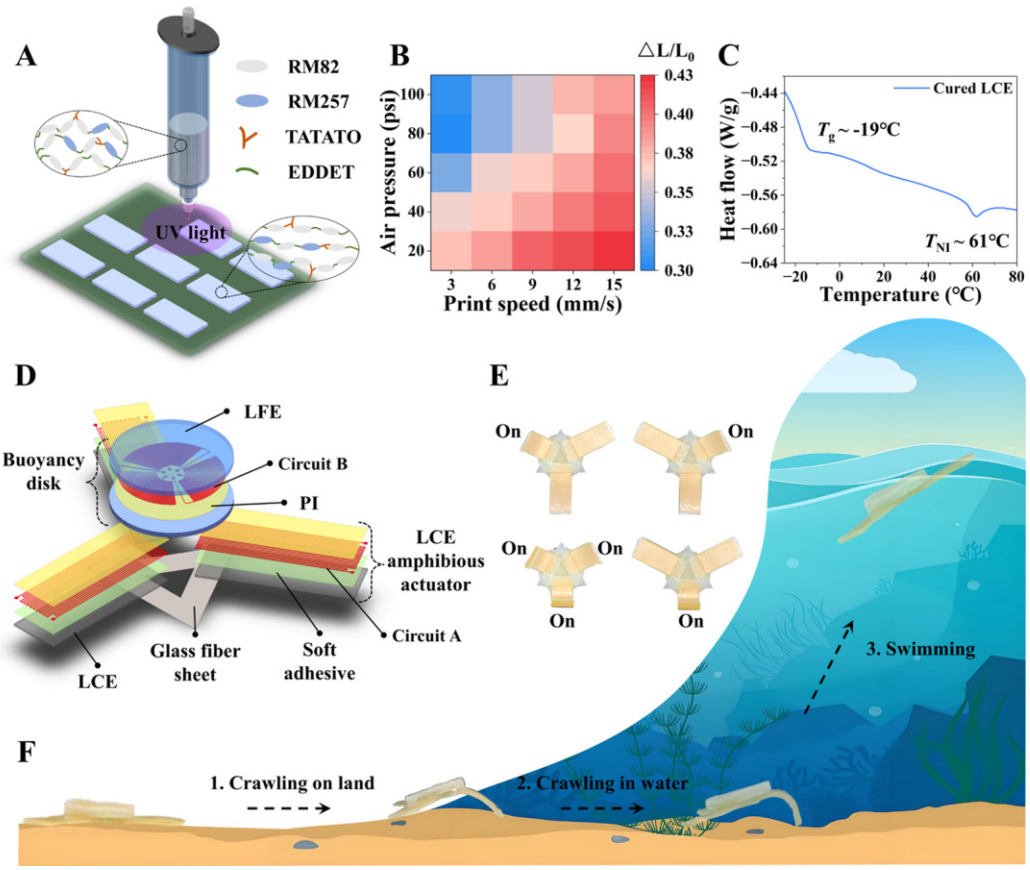

Figure 1. Design of the amphibious soft microrobot. (A) Schematic illustration of DIW printing with LCE ink (Movie S1). (B) Effect of printing air pressure and speed on LCE contraction strain (ΔL: contraction length upon actuation; L_0: original length). (C) DSC analysis of cured LCE inks. (D) Structural schematic of the microrobot. (E) Optical images showing sequential activation of LCE amphibious actuators inducing bending deformation. (F) Schematic of the microrobot's movement across different environments.

and photothermal effects[34,35] to Joule heating.[36,37] For example, Zadan et al. integrated LCEs with a deformable thermoelectric device to achieve bidirectional actuation,[38] while Zhao et al. employed a self-rolling LCE-based robot to navigate complex mazes via thermal activation.[39] Despite these advances, a single LCE actuator structure has yet to enable both land-based motion and efficient underwater swimming due to challenges in underwater thermal response, actuation control, and integration.

The primary obstacles to achieving efficient amphibious actuation include the limitations of optical drive—which complicates system control and integration—and the difficulties associated with underwater thermal actuation via Joule heating. To overcome these issues, we introduce a novel approach using 4D-printed LCE amphibious actuators (25 mm in length, 11 mm in width) integrated with flexible heating circuits (circuit A) capable of generating substantial thermal output. An external power supply, delivered via a 50 μm polyurethane-coated copper wire, drives these actuators to produce large deformation required for locomotion in both terrestrial and aquatic environments. With a length of 5 cm and a mass of 2.59 g, the resulting microrobot conforms to a commonly used classification for microrobots (length <15 cm, mass <20 g; see refs 10−13), while offering sufficient force and maneuverability through a structurally simple design suited for confined spaces.

Furthermore, to enable controlled underwater swimming, we develop a buoyancy-regulating disk inspired by the fish swim bladder. This disk, comprising two liquid-filled elastomer (LFE) and a secondary flexible heating circuit (circuit B), offers fine-tuned local buoyancy control with an adjustable range from 0 mN to 2.48 mN (for an LFE thickness of 3 mm). We evaluate the microrobot's performance through systematic characterization of its multidirectional movement, including underwater hovering at various depths, obstacle traversal, and navigation through narrow gaps. By integrating these innovative components, our amphibious soft microrobot demonstrates robust, multidirectional locomotion across complex environments, opening new avenues for applications in environmental monitoring and exploration.

EXPERIMENTAL SECTION

LCE Ink Synthesis. The LCE inks were synthesized using a modified thiol−acrylate "click" reaction, following a previously reported preparation method.[40] Briefly, 3.085 g of RM82 and 0.9 g of RM257 were preheated and dissolved in acetone. The solution was homogenized using a vortex mixer. Subsequently, 1.393 g of EDDET, 0.086 g of BHT, 0.201 g of TATATO, and 0.108 g of Irgacure 819 were added to the mixture and stirred for 10 min using a vortex mixer. Finally, 90 μL of the catalyst DPA was introduced, and the mixture was thoroughly homogenized. The resulting mixture was transferred into a 10 mL black syringe barrel and cured under vacuum at 65 °C for 3 h to form the oligomerized LCE ink.

Fabrication of Buoyancy Disks. The LFE was prepared by mixing Ecoflex 0050 with anhydrous ethanol. First, 20 wt % anhydrous ethanol (Beijing Tongguang Fine Chemical Co., Ltd.) was blended with part A of Ecoflex 0050, followed by thorough

https://doi.org/10.1021/acsami.5c08610
ACS Appl. Mater. Interfaces 2025, 17, 47456−47465

mixing with part B of Ecoflex 0050.[41] The resulting mixture was poured into molds fabricated using a Bambu Lab X1 3D printer (Figure S1B) and cured at room temperature for 3 h. The LFE layer had a diameter of 23 mm, which was 3 mm larger than the diameter of the circular flexible heating circuit to ensure proper alignment.

The buoyancy disk (density: 0.97 g/cm^3) was designed as a three-layer structure: LFE layers on the top and bottom, with a circular flexible heating circuit sandwiched in between. This configuration ensured efficient heat transfer from the heating circuit to the LFE, minimizing heat loss in the aqueous environment. The thickness of the bottom LFE layer was fixed at 1.5 mm, while the thickness of the top LFE layer was varied from 1.5 mm to 4.5 mm to adjust the initial buoyancy force, which ranged from 0.35 mN to 0.86 mN (Figure S21). For subsequent swimming experiments, the thicknesses of both the top and bottom LFE layers were fixed at 1.5 mm, although the structure could be further modified to meet specific application requirements.

For the substrate material, a glass fiber sheet (FR4, density: 1.7−2.2 g/cm^3) with excellent thermal stability was selected. A 200 μm thick glass fiber sheet was laser-cut into the desired shape (Figure S1A) and assembled with the buoyancy disk and LCE actuators for swimming tests.

Fabrication of Flexible Heating Circuits. The flexible heating circuits were fabricated using conventional flexible printed circuit board (FPCB) manufacturing methods, as illustrated in Figure S2.[42] The circuits were prepared using a polyimide copper laminate with a polyimide thickness of 12.5 μm and a copper coating thickness of 12 μm. A combination of image reversal optical lithography and wet etching techniques was employed to pattern the heating circuits on the polyimide copper laminate.

The fabrication process involved the following steps: (1) surface preparation: the copper surface was thoroughly cleaned, and a photographic dry film (Guangdong Taiyada Optoelectronics Co., Ltd., 38 μm) was laminated onto the surface. After removing air bubbles, the film was baked at 110 °C for 2 min (2) patterning: A photomask was aligned onto the dried dry film, and the assembly was exposed to UV light. The exposed film was then developed in a developer solution (Zhaoqing Zhiying Electronics Co., Ltd., developer-to-water ratio of 1:100). (3) Etching: The patterned polyimide copper laminate was immersed in a 10% sodium persulfate solution (Beijing Tongguang Fine Chemical Co., Ltd.) maintained at 60 °C for wet etching. (4) Cleaning: Residual etchant was removed using deionized water, and the photoresist was stripped using a release agent (Zhaoqing Zhiying Electronics Co., Ltd., release agent-to-water ratio of 1:60).

Two types of flexible heating circuits were fabricated. (1) Circuit A: rectangular circuits (25 mm × 11 mm) with a heating line width of 100 μm and a pitch of 100 μm (Figure S3A1,B1). These circuits were cut using a carbon dioxide laser cutter (Zing 24, Universal Laser Systems). (2) Circuit B: circular circuits with a diameter of 20 mm and the same heating line width and pitch as Circuit A (Figure S3A2,B2).

The initial resistances of circuits A and B were approximately 55 ohms and 20 ohms, respectively, and remained stable under cyclic bending and folding. The flexible heating circuits were bonded to the LCE amphibious actuators using a heat-resistant, flexible UV adhesive. Electrical connections were made using polyurethane-coated copper wires (50 μm copper diameter, 10 μm coating thickness, Shenzhen Dayuan Copper & Aluminum Materials Co., Ltd.), which were soldered to the circuits.

RESULTS AND DISCUSSION

Design of Amphibious Soft Microrobots with Underwater Swimming Capability. We develop the microrobot's motion structure using a homemade direct ink writing (DIW) 3D printer (Figures 1A, S4, and Movie S1, Supporting Information). In brief, the ink—comprising non-cross-linked liquid crystal (LC) oligomers (see Figure S5 for the molecular structures of RM82, RM258, TATATO, and EDDET)—is loaded into a black syringe and extruded through the DIW nozzle. The extruded LCE filaments are subsequently cross-linked under UV irradiation (≈2 mW cm^{-2}) to permanently fix their molecular alignment, followed by a full cure under higher intensity UV light (≈30 mW cm^{-2} for 15 min). Differential scanning calorimetry (DSC) confirms that the glass transition temperature T_g and the nematic−isotropic transition temperature T_{NI} of the cured LCE ink are −19 and 61 °C (Figure 1C). The relatively low T_{NI} is beneficial for its amphibious electrothermally driven actuation. Additional performance metrics are presented in Figures S6−S10.

As reported in prior studies,[40,43−46] key printing parameters (e.g., print speed, extrusion rate, temperature, layer height, and needle diameter) affect LCE molecular orientation and print quality. In our experiments, we fix the needle diameter at 0.6 mm, the layer height at 0.12 mm, and the printing temperature at 25 °C. We then optimize print quality and contraction strain by adjusting the printing speed and air pressure. Specifically, we observe that the contraction strain increases as air pressure decreases and printing speed increases (Figure 1B); however, excessively low pressure or high speed compromises print quality (Figures S11 and S12). An optimized combination of 12 mm/s and 60 psi achieves a contraction strain of approximately 40% while maintaining high print fidelity. The resulting LCE structures measure 25 mm in length, 11 mm in width, and 0.96 mm in thickness, as demonstrated in Movie S1.

The microrobot is actuated via Joule heating, a method chosen for its high controllability and real-time regulation of internal heat sources. The robot's architecture comprises three LCE amphibious actuators—arranged at 120° intervals—and a buoyancy-regulating disk designed to actively adjust local density (Figure 1D). Each LCE actuator consists of an LCE layer, a soft adhesive, and a flexible heating circuit (circuit A). Circuit A, fabricated from copper (∼12.0 μm thick) and polyimide (PI, ∼12.5 μm thick), has a total resistance of approximately 55 ohms (Figure S3A$_1$). A densely packed serpentine layout ensures uniform heat distribution, sufficient thermal output, and mechanical flexibility—allowing stable performance over repeated bending and folding cycles (Figure S3). As shown in Figure 1E, this configuration enables independent actuation of each limb, supports multidirectional movement, and produces large, reversible deformations via electrical heating.

Critical to underwater propulsion is the buoyancy-regulating disk, which consists of two liquid-filled elastomers (LFEs) and a second flexible heating circuit (circuit B). Circuit B features three fan-shaped sectors spaced 120° apart and exhibits a resistance of 20 ohms (Figure S3A2). Each sector adopts the same serpentine layout as circuit A, allowing for localized heating and dynamic tuning of the disk's density. This design enables the microrobot to generate controllable buoyant forces for swimming and hovering, supporting precise maneuvering in aquatic environments.

Finally, the LCE actuators and the buoyancy disk are mounted on a glass fiber plate, and power is supplied via thin, lightweight polyurethane-coated copper wires (50 μm) to minimize interference with underwater movement. Figure 1F schematically illustrates the seamless transition of the novel amphibious microrobot between terrestrial and aquatic locomotion, highlighting its multifunctional and controllable underwater movement, which opens up new possibilities for environmental monitoring and exploration in constrained or complex environments.

https://doi.org/10.1021/acsami.5c08610
ACS Appl. Mater. Interfaces 2025, 17, 47456−47465

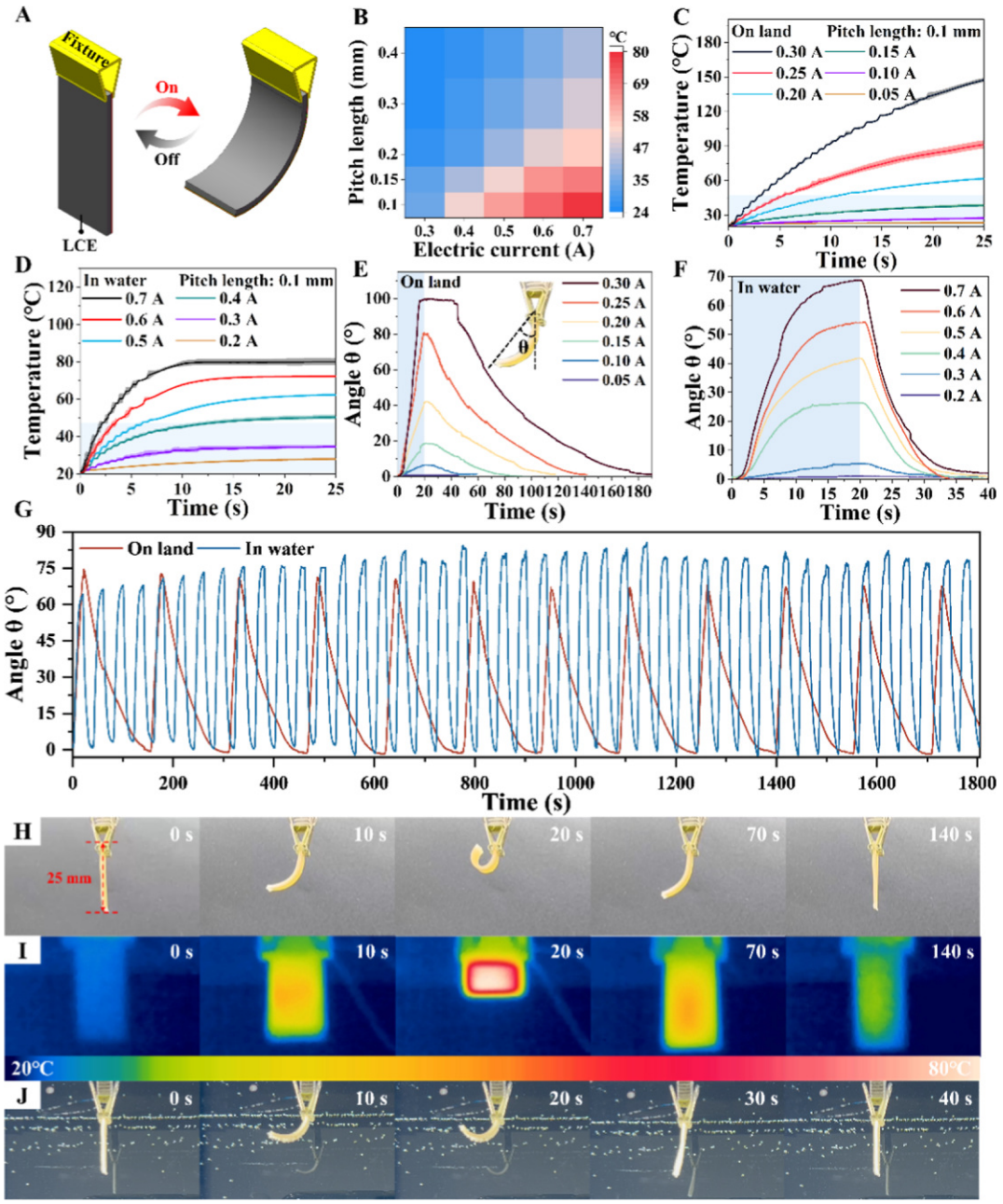

Figure 2. Design and characterization of LCE amphibious actuators. (A) Schematic diagram illustrating the thermally driven bending deformation of the LCE actuator. (B) The effect of the pitch length and input current of the heating circuit on the Joule heating (°C) of the actuator (C,D) Temperature−time curves recorded within the LCE actuator under different input currents applied on land (C) and in water (D). (E,F) Bending angle variation curves of the LCE actuator under different input currents on land (E) and in water (F). (G) Variation in bending angles over multiple reversible cycles following a 20 s current application and subsequent disconnection (recovery time: 120 s in air, 20 s in water). (H,J) Optical images showing the reversible bending of the LCE actuators under different input currents on land (H, Movie S2) and in water (J, Movie S2). (I) Infrared thermal image of the LCE actuator surface on land with a 0.25 A current applied.

Actuation Characteristics of LCE Amphibious Actuators. Figure 2A schematically illustrates the thermally driven bending deformation of our LCE actuator. Joule heating induces contraction in the LCE layer while the circuit A remains dimensionally stable under operating conditions, resulting in a bending motion toward the LCE side. To ensure that circuit A consistently heats the LCE actuator above its nematic−isotropic transition temperature T_{NI} in both air and water (Figure S14), we fix the circuit width and vary the pitch length from 0.1 mm to 0.4 mm across five distinct designs. Temperature rise profiles of these circuits are measured under various input currents (Figures 2B and S15). As the input current increases and the pitch length decreases, the operating temperature rises. Systematic optimization reveals that a 0.1 mm pitch, paired with input currents of 0.25 A on land and 0.7 A in water, provides the most effective heating, ensuring effective motion of the LCE actuators. This is attributed to the dense serpentine layout of circuit A, which ensures uniform heat distribution, sufficient thermal output, and mechanical flexibility (Figure S3).

Figure 2C,D presents the temperature−time curves recorded within the LCE amphibious actuator under different current

https://doi.org/10.1021/acsami.5c08610
ACS Appl. Mater. Interfaces 2025, 17, 47456−47465

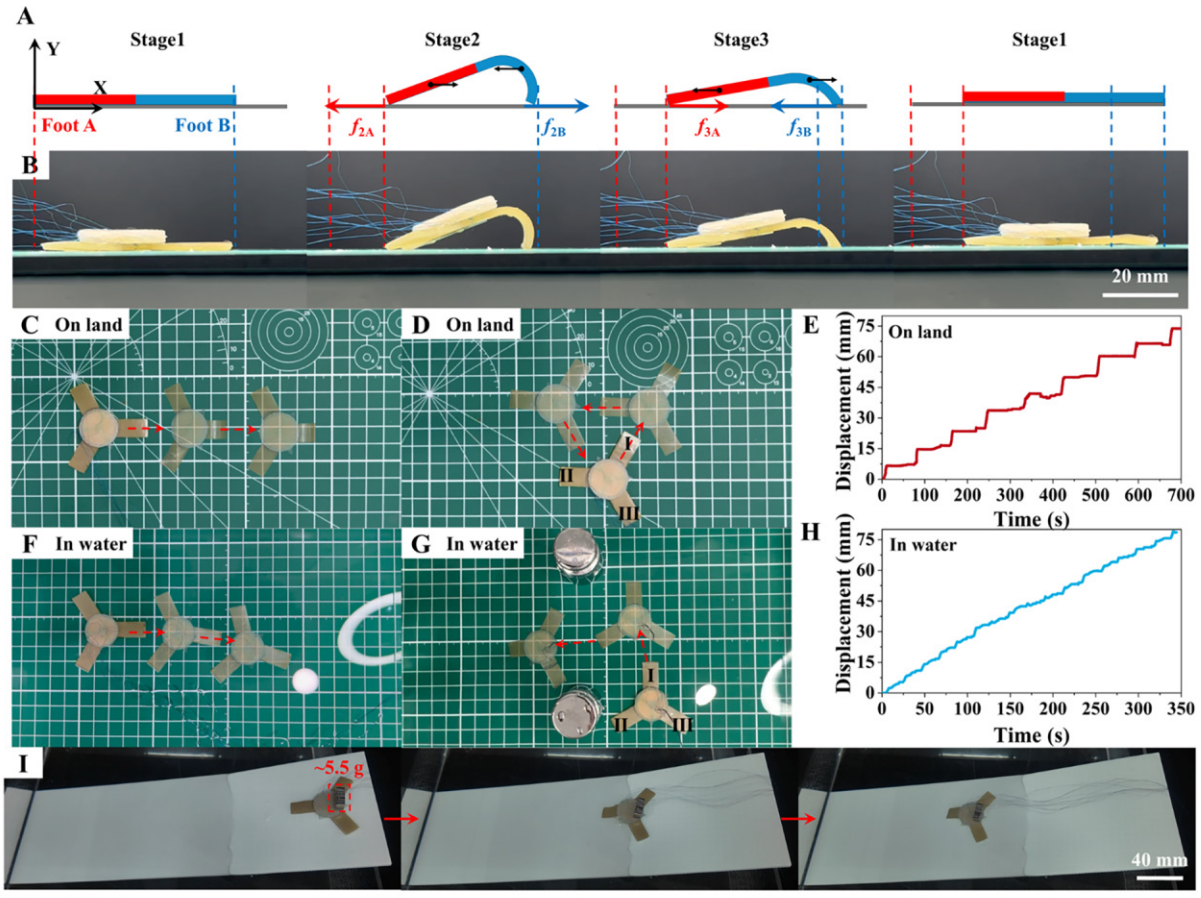

J

Refs.	11	21	22	30	31	32	34	35	36	37	38	43	This work
Land crawling (unidirectional)	√	√	√	√	√	√	×	×	√	√	√	√	√
Land crawling (multi-directional)	√	√	√	×	×	×	×	×	×	√	√	√	√
Swimming (unidirectional)	×	×	×	×	×	×	√	√	×	×	×	×	√
Swimming (multi-directional)	×	×	×	×	×	×	√	×	×	×	×	×	√
Wall climbing	√	×	×	×	×	×	×	×	×	×	×	×	×
Amphibious crawling (multi-directional)	×	×	×	×	×	×	×	×	×	×	×	×	√

Figure 3. Gait analysis and demonstration of the amphibious soft microrobot's movement. (A) Schematic diagram illustrating the crawling gait of the microrobot. (B) Physical diagram of the crawling configuration (Movie S3). (C) Unidirectional crawling on land (Movie S4) and the corresponding time−displacement curve (E). (D) Multidirectional crawling on land (Movie S5). (F) Unidirectional crawling in water (Movie S4) and the corresponding time−displacement curve (H). (G) Multidirectional crawling in water (Movie S5). (I) Seamless transition of the amphibious soft microrobot from land to water while carrying a 5.5 g payload, demonstrating robust amphibious locomotion and environmental adaptability (Movie S6). (J) Comparative chart of locomotion performance among thermally actuated soft robots.

conditions. Under a 20 s heating period, the internal temperatures reach 83.7 °C (0.25 A on land) and 79.9 °C (0.7 A in water), both exceeding T_{NI} of the LCE. In water, a temperature plateau around 10 s is observed due to heat absorption by the surrounding medium, which establishes a rapid balance between heating and dissipation. The polyimide (PI) film, with its excellent thermal resistance (up to 280 °C), remains unaffected by these elevated temperatures.

The actuator's bending behavior, as shown in Figure 2E,F, correlates with the applied current; higher currents induce larger bending angles. However, on land, applying 0.3 A for 20 s results in a plateau in bending angle due to contact with a fixed fixture, which limits further deformation. Moreover, excessively high currents can lead to prolonged cooling time, slow recovery, and potential structural damage, thereby compromising the microrobot's performance. At optimized current levels—0.25 A on land and 0.7 A in water—the LCE amphibious actuator exhibits stable, reversible bending over multiple cycles without failure or noticeable degradation (Figure 2G).

Optical images in Figure 2H,J (and Movie S2) capture the reversible bending of the LCE actuator under 0.25 A (land) and 0.7 A (water). After 20 s of heating, the maximum bending angles reached 80.7° on land and 68.7° in water. Once power is discontinued at 20 s, ambient cooling restored the actuator to its original vertical state, with recovery time of 120 s on land and 20 s in water (Figure S16). Additionally, the infrared thermal image in Figure 2I confirms the uniform heating provided by the circuit A. Overall, these results demonstrate that our LCE amphibious actuator offers excellent thermal driving performance, ensuring reliable actuation that underpins the subsequent locomotion of the amphibious soft microrobot.

Gait Analysis and Demonstration of Amphibious Motion. To elucidate the crawling mechanism of the

https://doi.org/10.1021/acsami.5c08610
ACS Appl. Mater. Interfaces 2025, 17, 47456−47465

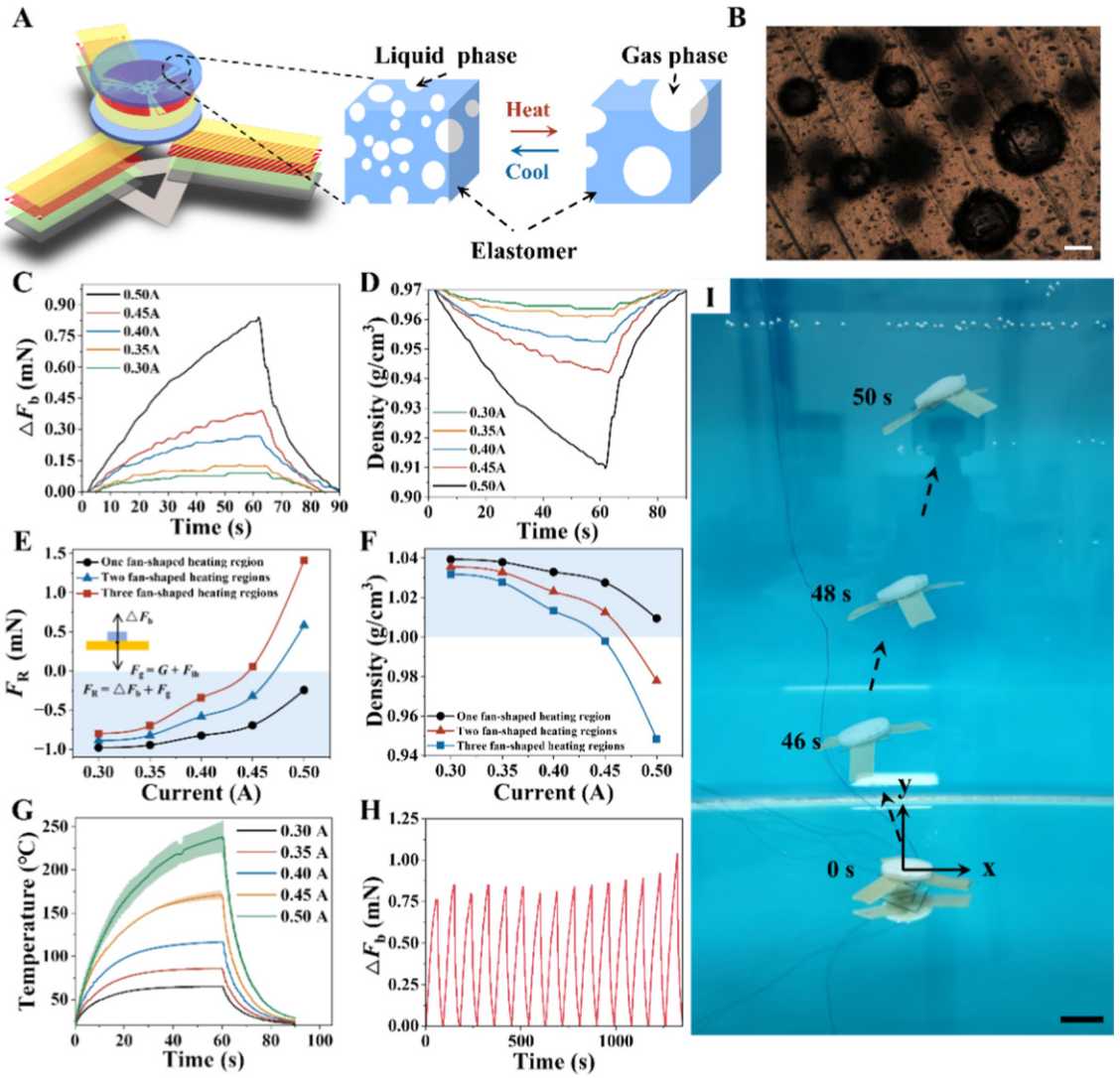

Figure 4. Design and characterization of the buoyancy disk for the amphibious soft microrobot. (A) Schematic of the density modulation mechanism via the liquid-to-gas phase transition of the elastomer-coated liquid upon heating. (B) Optical image of the disk interior. (C,D) Curves of the buoyant force generation ΔF_b (C) and corresponding density changes (D) for a 3 mm-thick disk under different input currents. (E,F) Active adjustment of the robot's resultant force F_R (E) and overall density (F) in water (a 0.5 A current was applied to uniformly heat one, two, or three fan-shaped regions). Here, F_R, ΔF_b, F_g, G, and F_{ib} denote the resultant force acting on the robot, the disk buoyancy, the initial resultant force acting on the robot, the robot's gravity, and the initial buoyancy of the robot, respectively. (G) Temperature variation curves for a fan-shaped heating region under input currents. (H) Buoyancy variation curve of a 3 mm-thick disk under a 0.5 A alternating current (60 s heating, 30 s cooling). (I) The microrobot swimming upward underwater, driven by an increase in uniform buoyant force ΔF_b generated via 0.5 A current applied to all three heating regions (Movie S7). Scale bars, 200 μm in (B) and 2 cm in (I).

amphibious soft microrobot—driven by the reversible deformation of its LCE amphibious actuators—we conduct a comprehensive mechanical analysis of its gait (Figure S17). We simplify the microrobot into two distinct parts (red and blue) and designate its front and rear contact points as foot A and foot B, respectively (Figure 3A,B and Movie S3). The friction between these contact points and the substrate is the primary factor governing the crawling motion. In our heat-induced actuation, a differential friction force between foot A and foot B is critical for forward motion. To ensure that foot B remains stationary while foot A advances, a glass fiber sheet is incorporated as a substrate at the robot's base, thereby creating the necessary frictional differential (Figure 1D).

Under idealized conditions, we define foot A as the origin, with the positive x-axis corresponding to the direction of movement. The crawling cycle was divided into three stages: stage 1 (heating), stage 2 (contraction), and stage 3 (extension). In stage 1, upon power application, the blue section is uniformly heated above the nematic−isotropic transition temperature T_{NI}, initiating actuation without inducing sliding between the contact points. In stage 2, the bending of the blue LCE actuator pulls the red section forward. Due to asymmetry in the contact areas, the sliding friction force f_{2A} at foot A reaches the threshold required for sliding earlier than that at foot B (f_{2B}), causing foot A to slide forward while foot B remains stationary. In stage 3, once power is removed, the blue section cools below T_{NI} and recovers its original shape. This reversal in geometry switches the frictional forces (f_{3A} and f_{3B}), allowing foot B to reach the sliding threshold and advance while foot A remains stationary, thus completing a full crawling cycle. Notably, the heating and contraction phases (stages 1 and 2) last approximately 12 s on

https://doi.org/10.1021/acsami.5c08610
ACS Appl. Mater. Interfaces 2025, 17, 47456−47465

land (9 s in water), whereas the extension phase (stage 3) takes about 60 s on land (15 s in water) due to the slower rate of heat dissipation. Comparable locomotion is observed in both environments, with variations attributable to differing friction coefficients and buoyancy effects.

The stability of the robot's gait is highly sensitive to the applied current. We found that currents of 0.25 A on land and 0.7 A in water optimized crawling performance. On land, a 0.3 A current led to overly rapid heating—resulting in excessive curling and hindering recovery—while 0.2 A produced insufficient bending for effective locomotion. In water, currents above 0.7 A compromised the integrity of the 50 μm polyurethane-coated copper wire, whereas 0.6 A proved similarly ineffective locomotion.

Optical images (Figure 3C,F and Movie S4) confirm the unidirectional crawling of the microrobot on both land and water. Displacement−time curves (Figure 3E,H) indicate average step lengths of approximately 8.79 mm on land and 3.86 mm in water per crawling cycle. Moreover, by integrating three LCE amphibious actuators (Figure 1E), the microrobot achieves multidirectional crawling. Optical observations (Figure 3D and Movie S5) reveal a triangular crawling path on land, accomplished by sequentially activating LCE amphibious actuators I, II, and III, thereby returning the robot to its initial position. In water, the coordinated activation of actuators I and II enables turning maneuvers (Figure 3G and Movie S5).

We further evaluated the robot's amphibious performance by examining its seamless transition between terrestrial and aquatic environments and its load-carrying capability (Figure 3I and Movie S6). The results show that the robot can reliably transition from land to water while carrying a 5.5 g payload, highlighting its robust amphibious locomotion and strong environmental adaptability.

In addition to flat surfaces, the microrobot successfully navigated an inclined ratchet surface with a 20° slope (Figure S18 and Movie S6). These amphibious and multidirectional capabilities distinguish our soft microrobot from most previously reported systems—which often lack either amphibious functionality or multidirectional mobility (Figure 3J and Table S1)—and underscore its potential for applications such as search and rescue.

Design and Characterization of the Microrobot with Underwater Swimming Capability. To achieve controllable buoyant motion in water, we engineer a buoyancy disk for the amphibious soft microrobot by fabricating a liquid-filled elastomer (LFE) using Ecoflex 0050 as the base material and ethanol as the filler. Joule heating is employed to actively modulate the local density of the LFE, thereby providing adjustable buoyancy (Figure 4A). The buoyancy disk is composed of two LFEs that sandwich a flexible heating circuit (circuit B) (Figure 1D). This mechanism is analogous to the density regulation observed in whales—where fat layers contract to increase density and expand to decrease density[47−49]—with the key distinction that, in our design, ethanol is thermally induced to transition from a liquid to a gaseous state. When an appropriate current is applied to circuit B, sufficient heat is generated to raise the internal temperature of the buoyancy disk above ethanol's boiling point. The resultant vaporization causes the elastomer matrix to expand, thereby increasing the disk's volume and reducing its density (Figures 4A and S19−S21). Figure 4B shows an optical image of ethanol encapsulated within the elastomer in the LFE layer.

To minimize the impact on underwater locomotion and ensure durability under high-current conditions, we use 50 μm polyurethane-coated copper wires. Both the LFE and circuit B are circular in geometry and assembled in an axisymmetric configuration (LFE, flexible heating circuit, LFE) (Figure 1D). The LFE's diameter (23 mm) exceeds that of circuit B (20 mm), ensuring complete encapsulation and protection from water ingress. Circuit B features three equally sized fan-shaped heating regions (Figure S13A2) that enable simultaneous, real-time heating at multiple locations, ensuring uniform heat distribution and consistent modulation of the LFE's volume.

Real-time control of the LFE's volume—and consequently its density and buoyancy—is achieved via active heating. Figure 4G shows the internal temperature variations of the underwater buoyancy disk under different input currents. When one of the fan-shaped heating regions is activated, a buoyant force change ΔF_b is induced; corresponding density variations are detailed in Figure 4C,D. The sector heating zone of the circuit B during the buoyancy test is shown in Figure S22A. After approximately 60 s of heating, ΔF_b reaches a maximum of 0.827 mN, reducing the disk's density to a minimum of 0.910 g/cm^3. Upon cooling for about 30 s, ΔF_b gradually returns to 0 mN as the density increases to a maximum of 0.97 g/cm^3. Figure S20 illustrates the changes in the buoyant force (ΔF_b) and density of activated buoyant disks with thicknesses of 4 mm, 5 mm, and 6 mm.[50] Notably, the buoyancy changes are highly repeatable (Figure 4H).

We further investigate the influence of LFE thickness on the initial buoyancy. Buoyancy disks with thicknesses of 3 mm, 4 mm, 5 mm, and 6 mm exhibit varying initial buoyancies, increasing from 0.35 mN to 0.86 mN as thickness increases (Figure S21). Buoyant disks of varying thicknesses provide the microrobot with a range of buoyancy adjustments, enabling it to perform multiple tasks effectively, such as navigating different fluid environments or adapting to varying payloads. For example, when a 6 mm-thick buoyancy disc is employed, simultaneous activation of all three sector-shaped heating regions generates a maximum buoyancy change ΔF_b of 8.31 mN, allowing the amphibious soft microrobot to carry a load of approximately 0.791 g in water. For subsequent swimming experiments, a 3 mm thick buoyancy disk is selected. By varying the input current, one or more fan-shaped heating regions can be activated to regulate the overall resultant force F_R and the microrobot's density (Figure 4E,F). In our design, the overall density of the microrobot exceeds 1 g/cm^3, ensuring that it sinks when inactive. A current between 0.3 and 0.5 A is applied to activate the heating regions; for instance, a 0.5 A current applied to coupled pairs of two or three regions reduces the microrobot's density from 1.043 g/cm^3 to 0.977 g/cm^3 (or 0.948 g/cm^3), respectively (Figure 4F). When the microrobot is stationary underwater, its gravitational force is approximately 1.07 mN. Once ΔF_b reaches around 1.07 mN, the microrobot begins to swim upward (Figure 4E).

As demonstrated in Figures 4I and Movie S7, as well as Movie S7, after applying a 0.5 A current to simultaneously activate all three fan-shaped heating regions, the amphibious soft microrobot exhibits steady upward swimming at a speed of approximately 43.5 mm/s (~10 body thickness per second), facilitating rapid underwater exploration with enhanced efficiency.

Underwater Swimming Motion. Leveraging the buoyancy disk design that enables active local density modulation (Figure 1D), our amphibious soft microrobot not only

https://doi.org/10.1021/acsami.5c08610
ACS Appl. Mater. Interfaces 2025, 17, 47456−47465

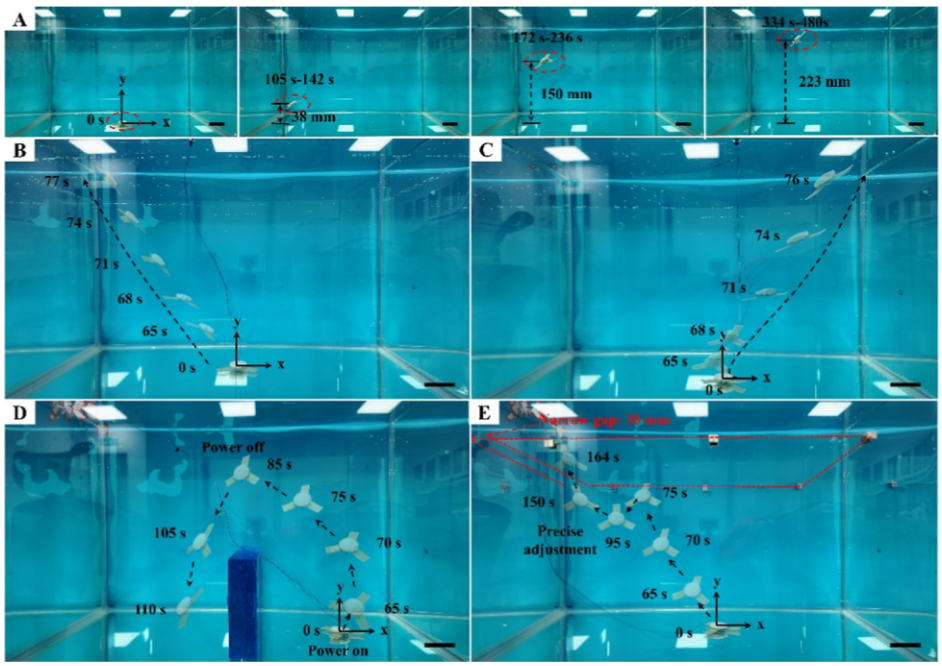

Figure 5. Demonstration of underwater swimming of the amphibious soft microrobot. Experimental water tank dimensions are 45 cm × 28 cm × 30 cm. (A) the microrobot hovering at the bottom, middle, and top of the tank (Movie S8). Composite images of the amphibious microrobot swimming in the negative *x*-direction (B, Movie S9) and positive *x*-direction (C, Movie S9). (D) Composite image of the microrobot overcoming an underwater obstacle of height 10 cm and width 3 cm (Movie S10). (E) Composite image of the microrobot passing through a narrow gap of width 30 mm (Movie S11). Scale bars, 4 cm.

achieves underwater crawling but also exhibits robust multidirectional swimming, thereby expanding its potential applications. The fan-shaped heating regions corresponding to circuit B during the swimming demonstration of the amphibious soft microrobot is shown in Figure S24. To validate its underwater performance, we first assess the robot's hovering capability at different depths. As shown in Figures 5A, S24A and Movie S8, simultaneous application of a 0.5 A current to the two fan-shaped heating regions of the buoyancy disk initially propelled the microrobot upward. By subsequently reducing the input current to approximately 0.473 A—corresponding to an overall density near 1 g/cm^3 (Figure 4F)—we are able to stabilize its vertical position. At different depths, the microrobot maintains hovering for approximately 64 s in the midtank region and 146 s near the top, demonstrating precise depth control via current modulation.

The robot's multidirectional swimming capabilities are also evaluated. Overlaid image sequences (Figures 5B and S24B, and Movie S9) reveal controlled swimming from the tank center toward the negative *x*-direction, while side-swimming toward the positive *x*-direction is captured in Figure 5C and Movie S9 under a 0.5 A current. Directional control is achieved through the selective activation of any two fan-shaped heating regions on the buoyancy disk, which induces localized thermal expansion and generates an asymmetric distribution of buoyant forces. This asymmetry produces a net propulsive force oriented along the bisector of the activated regions, propelling the amphibious soft microrobot in the desired direction (Figure S24). These results confirm that reliable directional swimming can be achieved through spatially resolved activation of the buoyancy control system.

Furthermore, the enhanced swimming capabilities enable effective obstacle negotiation. As illustrated in Figures 5D and S24D, and Movie S10, the microrobot successfully overcomes a 10 cm high obstacle. After ascending past the obstacle, power is removed, and the microrobot continues its descent along the negative *x*-direction until it comes to rest at the tank's bottom, indicating a repeatable and robust maneuver.

Finally, the microrobot demonstrates the ability to traverse narrow underwater gaps. In a test where the robot (5 cm in size) is required to pass through a 3 cm-wide opening (Figures 5E and S24E, and Movie S11), precise adjustment of the input current allows gradual buoyancy modulation, ultimately enabling the entire body to clear the gap.

In summary, our novel amphibious soft microrobot integrates both crawling and multidirectional underwater swimming, overcoming the limitations of many existing soft robots that are confined to a single environment or locomotion mode. As detailed in Table S1, our system demonstrates notable advantages in environmental adaptability and motion diversity, presenting a promising platform for exploration and reconnaissance in complex terrains.

CONCLUSION

This study presents a novel amphibious soft microrobot capable of versatile, multimodal locomotion across land and water. By integrating 4D-printed liquid crystal elastomers (LCEs) with a flexible heating circuit, we fabricate LCE amphibious actuators that generate large deformation, enabling robust movement across diverse land and water environments. A specially designed buoyancy disk—comprising two liquid-filled elastomer and a separate heating circuit—allows precise density modulation for active buoyancy control, providing robust support for the robot's controlled underwater locomotion. Comprehensive performance characterization demonstrates multidirectional crawling, controllable swimming, depth hovering, obstacle crossing, and navigation through narrow gaps, underscoring the microrobot's potential

https://doi.org/10.1021/acsami.5c08610
ACS Appl. Mater. Interfaces 2025, 17, 47456−47465

for advanced monitoring and exploration in complex environments. This design not only facilitates seamless transitions between land and water but also opens promising avenues for environmental monitoring and exploration using soft, deformable robotic systems. Such advances lay the foundation for integrating these systems into intelligent autonomous platforms, enhancing adaptability and functionality in diverse and challenging environments.

Despite its strong potential, the current system remains at a developmental stage and faces challenges that limit its practical deployment. Chief among these are reliance on an external power source and reduced swimming stability in turbulent aquatic environments. Future work will focus on improving untethered operation, enhancing environmental robustness, and scaling down system size to increase autonomy and applicability in real-world, dynamic settings.

■ ASSOCIATED CONTENT

Supporting Information

The Supporting Information is available free of charge at https://pubs.acs.org/doi/10.1021/acsami.5c08610.

Detailed information on the materials, experimental procedures, relevant data sets, and photographic documentation (PDF)

Direct ink writing-based 4D printing of liquid crystal elastomer (LCE) ink. Movie S1 (MP4)

Bending angle response of the LCE amphibious actuator to varying input currents on land and in water. Movie S2 (MP4)

A crawling cycle of the amphibious soft microrobot. Movie S3 (MP4)

Unidirectional and multidirectional crawling of the amphibious soft microrobot on land. Movie S4 (MP4)

Unidirectional and multidirectional crawling of the amphibious soft microrobot in water. Movie S5 (MP4)

Transition of the amphibious soft microrobot from land to water while carrying a 5.5 g payload, and climbing performance on land and in water. Movie S6 (MP4)

Vertical swimming of the amphibious soft microrobot in water. Movie S7 (MP4)

Hovering behavior of the amphibious soft microrobot at different water depths. Movie S8 (MP4)

Swimming of the amphibious soft microrobot along *x*-direction in water. Movie S9 (MP4)

The amphibious soft microrobot crossing an obstacle via swimming. Movie S10 (MP4)

The amphibious soft microrobot navigating through a narrow gap underwater. Movie 11 (MP4)

■ AUTHOR INFORMATION

Corresponding Author

Xin Yi − *School of Mechanics and Engineering Science, Peking University, Beijing 100871, China;* orcid.org/0000-0002-4726-5765; Email: xyi@pku.edu.cn

Authors

Chenglin Li − *School of Mechanics and Engineering Science, Peking University, Beijing 100871, China*

Jing Li − *School of Mechanics and Engineering Science, Peking University, Beijing 100871, China*

Complete contact information is available at: https://pubs.acs.org/10.1021/acsami.5c08610

Author Contributions

This manuscript was written through the contributions of all authors. All authors have given approval to the final version of the manuscript.

Notes

The authors declare no competing financial interest.

■ ACKNOWLEDGMENTS

This work was supported by the National Natural Science Foundation of China (12272004).

■ REFERENCES

(1) Patel, D. K.; Huang, X.; Luo, Y.; Mungekar, M.; Jawed, M. K.; Yao, L.; Majidi, C. Highly Dynamic Bistable Soft Actuator for Reconfigurable Multimodal Soft Robots. *Adv. Mater. Technol.* **2023**, *8*, 2201259.

(2) Wu, J.; Wu, M.; Chen, W.; Wang, C.; Xie, G. Multimodal Soft Amphibious Robots Using Simple Plastic-Sheet-Reinforced Thin Pneumatic Actuators. *IEEE Trans. Robot.* **2024**, *40*, 1874−1889.

(3) Gong, S.; Fang, F.; Yi, Z.; Feng, B.; Li, A.; Li, W.; Shao, L.; Zhang, W. An Intelligent Spinal Soft Robot with Self-Sensing Adaptability. *Innovation* **2024**, *5*, 100640.

(4) Fang, F.; Zhou, J.; Zhang, Y.; Yi, Y.; Huang, Z.; Feng, Y.; Tao, K.; Li, W.; Zhang, W. A Multimodal Amphibious Robot Driven by Soft Electrohydraulic Flippers. *Cyborg Bionic Syst.* **2025**, *6*, 0253.

(5) Xiong, Q.; Zhou, X.; Li, D.; Ambrose, J. W.; Yeow, R. C. An Amphibious Fully-Soft Centimeter-Scale Miniature Crawling Robot Powered by Electrohydraulic Fluid Kinetic Energy. *Adv. Sci.* **2024**, *11*, 2308033.

(6) Cohen, A.; Zarrouk, D. The AmphiSTAR High Speed Amphibious Sprawl Tuned Robot: Design and Experiments. In *2020 IEEE/RSJ. International Conference on Intelligent Robots and Systems*; IEEE: Las Vegas, NV, USA, 2020, pp 6411−6418.

(7) Kim, C.; Lee, K.; Ryu, S.; Seo, T. Amphibious Robot With Self-Rotating Paddle-Wheel Mechanism. *IEEE/ASME Trans. Mechatron.* **2023**, *28*, 1836−1843.

(8) Wang, W.; Yu, J.; Ding, R.; Tan, M. Bio-Inspired Design and Realization of a Novel Multimode Amphibious Robot. In *2009 IEEE International Conference on Automation and Logistics*; IEEE: Shenyang, China, 2009, pp 140−145.

(9) Liang, X.; Xu, M.; Xu, L.; Liu, P.; Ren, X.; Kong, Z.; Yang, J.; Zhang, S. The AmphiHex: A Novel Amphibious Robot with Transformable Leg-Flipper Composite Propulsion Mechanism. In *2012 IEEE/RSJ. International Conference on Intelligent Robots and Systems*; IEEE: Vilamoura-Algarve, Portugal, 2012, pp 3667−3672.

(10) De Rivaz, S. D.; Goldberg, B.; Doshi, N.; Jayaram, K.; Zhou, J.; Wood, R. J. Inverted and Vertical Climbing of a Quadrupedal Microrobot Using Electroadhesion. *Sci. Robot.* **2018**, *3*, No. eaau3038.

(11) Pang, W.; Xu, S.; Wu, J.; Bo, R.; Jin, T.; Xiao, Y.; Liu, Z.; Zhang, F.; Cheng, X.; Bai, K.; Song, H.; Xue, Z.; Wen, L.; Zhang, Y. A Soft Microrobot with Highly Deformable 3D Actuators for Climbing and Transitioning Complex Surfaces. *Proc. Natl. Acad. Sci. U.S.A.* **2022**, *119*, No. e2215028119.

(12) Lai, Y.; Zang, C.; Luo, G.; Xu, S.; Bo, R.; Zhao, J.; Yang, Y.; Jin, T.; Lan, Y.; Wang, Y.; Wen, L.; Pang, W.; Zhang, Y. An Agile Multimodal Microrobot with Architected Passively Morphing Wheels. *Sci. Adv.* **2024**, *10*, No. eadp1176.

(13) Chen, Y.; Doshi, N.; Goldberg, B.; Wang, H.; Wood, R. J. Controllable Water Surface to Underwater Transition through Electrowetting in a Hybrid Terrestrial-Aquatic Microrobot. *Nat. Commun.* **2018**, *9*, 2495.

(14) Li, T.; Yu, S.; Sun, B.; Li, Y.; Wang, X.; Pan, Y.; Song, C.; Ren, Y.; Zhang, Z.; Grattan, K. T. .; Wu, Z.; Zhao, J. Bioinspired Claw-Engaged and Biolubricated Swimming Microrobots Creating Active Retention in Blood Vessels. *Sci. Adv.* **2023**, *9*, No. eadg4501.

(15) Luo, Y.; Patel, D. K.; Li, Z.; Hu, Y.; Luo, H.; Yao, L.; Majidi, C. Intrinsically Multistable Soft Actuator Driven by Mixed-Mode Snap-Through Instabilities. *Adv, Sci.* **2024**, *11*, 2307391.
(16) Cheng, Z.; Feng, W.; Zhang, Y.; Sun, L.; Liu, Y.; Chen, L.; Wang, C. A Highly Robust Amphibious Soft Robot with Imperceptibility Based on a Water-Stable and Self-Healing Ionic Conductor. *Adv. Mater.* **2023**, *35*, 2301005.
(17) Zhang, Z.; Wang, L.; Jiang, F.; Yu, S.; Ji, F.; Sun, T.; Zhang, H.; Zhu, Y.; Chang, H.; Li, T.; Zhao, J. Fully Integrated Wearable Control System for Micro/Nanorobot Navigation. *Int. J. Extrem. Manuf.* **2025**, *7*, 035505.
(18) Wang, Q.; Wang, Q.; Ning, Z.; Chan, K. F.; Jiang, J.; Wang, Y.; Su, L.; Jiang, S.; Wang, B.; Ip, B. Y. M.; Ko, H.; Leung, T. W. H.; Chiu, P. W. Y.; Yu, S. C. H.; Zhang, L. Tracking and Navigation of a Microswarm under Laser Speckle Contrast Imaging for Targeted Delivery. *Sci. Robot.* **2024**, *9*, No. eadh1978.
(19) Zhang, S.; Mou, F.; Yu, Z.; Li, L.; Yang, M.; Zhang, D.; Ma, H.; Luo, W.; Li, T.; Guan, J. Heterogeneous Sensor-Carrier Microswarms for Collaborative Precise Drug Delivery toward Unknown Targets with Localized Acidosis. *Nano Lett.* **2024**, *24*, 5958−5967.
(20) Zhao, Y.; Chi, Y.; Hong, Y.; Li, Y.; Yang, S.; Yin, J. Twisting for Soft Intelligent Autonomous Robot in Unstructured Environments. *Proc. Natl. Acad. Sci. U.S.A.* **2022**, *119*, No. e2200265119.
(21) Wu, S.; Hong, Y.; Zhao, Y.; Yin, J.; Zhu, Y. Caterpillar-Inspired Soft Crawling Robot with Distributed Programmable Thermal Actuation. *Sci. Adv.* **2023**, *9*, No. eadf8014.
(22) He, Q.; Wang, Z.; Wang, Y.; Minori, A.; Tolley, M. T.; Cai, S. Electrically Controlled Liquid Crystal Elastomer−Based Soft Tubular Actuator with Multimodal Actuation. *Sci. Adv.* **2019**, *5*, No. eaax5746.
(23) Chen, Y.; Valenzuela, C.; Liu, Y.; Yang, X.; Yang, Y.; Zhang, X.; Ma, S.; Bi, R.; Wang, L.; Feng, W. Biomimetic Artificial Neuromuscular Fiber Bundles with Built-in Adaptive Feedback. *Matter* **2025**, *8*, 101904.
(24) Feng, X.; Wang, L.; Xue, Z.; Xie, C.; Han, J.; Pei, Y.; Zhang, Z.; Guo, W.; Lu, B. Melt Electrowriting Enabled 3D Liquid Crystal Elastomer Structures for Cross-Scale Actuators and Temperature Field Sensors. *Sci. Adv.* **2024**, *10*, No. eadk3854.
(25) Li, S.; Wang, Y.; Liu, Z.; Chen, B.; Liu, M.; He, X.; Yang, S. Flexible Pyroelectric Energy Harvesters from Nanocomposites of Liquid Crystal Elastomers/Lead Zirconate Titanate Nanoparticles. *Sci. Adv.* **2025**, *11*, No. eadt6136.
(26) Vinciguerra, M. R.; Patel, D. K.; Zu, W.; Tavakoli, M.; Majidi, C.; Yao, L. Multimaterial Printing of Liquid Crystal Elastomers with Integrated Stretchable Electronics. *ACS Appl. Mater. Interfaces* **2023**, *15*, 24777−24787.
(27) Chen, W.; Tong, D.; Meng, L.; Tan, B.; Lan, R.; Zhang, Q.; Yang, H.; Wang, C.; Liu, K. Knotted Artificial Muscles for Bio-Mimetic Actuation under Deepwater. *Adv. Mater.* **2024**, *36*, 2400763.
(28) Cui, B.; Ren, M.; Dong, L.; Wang, Y.; He, J.; Wei, X.; Zhao, Y.; Xu, P.; Wang, X.; Di, J.; Li, Q. Pretension-Free and Self-Recoverable Coiled Artificial Muscle Fibers with Powerful Cyclic Work Capability. *ACS Nano* **2023**, *17*, 12809−12819.
(29) Leanza, S.; Lu-Yang, J.; Kaczmarski, B.; Wu, S.; Kuhl, E.; Zhao, R. R. Elephant Trunk Inspired Multimodal Deformations and Movements of Soft Robotic Arms. *Adv. Funct. Mater.* **2024**, *34*, 2400396.
(30) Wang, Y.; Yin, R.; Jin, L.; Liu, M.; Gao, Y.; Raney, J.; Yang, S. 3D-Printed Photoresponsive Liquid Crystal Elastomer Composites for Free-Form Actuation. *Adv. Funct. Mater.* **2023**, *33*, 2210614.
(31) Xiao, Y.; Jiang, Z.; Tong, X.; Zhao, Y. Biomimetic Locomotion of Electrically Powered "Janus" Soft Robots Using a Liquid Crystal Polymer. *Adv. Mater.* **2019**, *31*, 1903452.
(32) Ren, L.; He, Y.; Wang, B.; Xu, J.; Wu, Q.; Wang, Z.; Li, W.; Ren, L.; Zhou, X.; Liu, Q.; Li, B.; Song, Z. 4D Printed Self-Sustained Soft Crawling Machines Fueled by Constant Thermal Field. *Adv. Funct. Mater.* **2024**, *34*, 2400161.
(33) Kotikian, A.; McMahan, C.; Davidson, E. C.; Muhammad, J. M.; Weeks, R. D.; Daraio, C.; Lewis, J. A. Untethered Soft Robotic Matter with Passive Control of Shape Morphing and Propulsion. *Sci. Robot.* **2019**, *4*, No. eaax7044.
(34) Wang, Y.; Xuan, H.; Zhang, L.; Huang, H.; Neisiany, R. E.; Zhang, H.; Gu, S.; Guan, Q.; You, Z. 4D Printed Non-Euclidean-Plate Jellyfish Inspired Soft Robot in Diverse Organic Solvents. *Adv. Mater.* **2024**, *36*, 2313761.
(35) Sartori, P.; Yadav, R. S.; Del Barrio, J.; DeSimone, A.; Sánchez-Somolinos, C. Photochemically Induced Propulsion of a 4D Printed Liquid Crystal Elastomer Biomimetic Swimmer. *Adv. Sci.* **2024**, *11*, 2308561.
(36) Ford, M. J.; Ambulo, C. P.; Kent, T. A.; Markvicka, E. J.; Pan, C.; Malen, J.; Ware, T. H.; Majidi, C. A Multifunctional Shape-Morphing Elastomer with Liquid Metal Inclusions. *Proc. Natl. Acad. Sci. U.S.A.* **2019**, *116*, 21438−21444.
(37) Wang, C.; Sim, K.; Chen, J.; Kim, H.; Rao, Z.; Li, Y.; Chen, W.; Song, J.; Verduzco, R.; Yu, C. Soft Ultrathin Electronics Innervated Adaptive Fully Soft Robots. *Adv. Mater.* **2018**, *30*, 1706695.
(38) Zadan, M.; Patel, D. K.; Sabelhaus, A. P.; Liao, J.; Wertz, A.; Yao, L.; Majidi, C. Liquid Crystal Elastomer with Integrated Soft Thermoelectrics for Shape Memory Actuation and Energy Harvesting. *Adv. Mater.* **2022**, *34*, 2200857.
(39) Zhao, Y.; Hong, Y.; Li, Y.; Qi, F.; Qing, H.; Su, H.; Yin, J. Physically Intelligent Autonomous Soft Robotic Maze Escaper. *Sci. Adv.* **2023**, *9*, No. eadi3254.
(40) Saed, M. O.; Ambulo, C. P.; Kim, H.; De, R.; Raval, V.; Searles, K.; Siddiqui, D. A.; Cue, J. M. O.; Stefan, M. C.; Shankar, M. R.; Ware, T. H. Molecularly-Engineered, 4D-Printed Liquid Crystal Elastomer Actuators. *Adv. Funct. Mater.* **2019**, *29*, 1806412.
(41) Miriyev, A.; Stack, K.; Lipson, H. Soft Material for Soft Actuators. *Nat. Commun.* **2017**, *8*, 596.
(42) Richter, M.; Sikorski, J.; Makushko, P.; Zabila, Y.; Venkiteswaran, V. K.; Makarov, D.; Misra, S. Locally Addressable Energy Efficient Actuation of Magnetic Soft Actuator Array Systems. *Adv. Sci.* **2023**, *10*, 2302077.
(43) Maurin, V.; Chang, Y.; Ze, Q.; Leanza, S.; Wang, J.; Zhao, R. R. Liquid Crystal Elastomer − Liquid Metal Composite: Ultrafast, Untethered, And Programmable Actuation by Induction Heating. *Adv. Mater.* **2024**, *36*, 2302765.
(44) Peng, X.; Wu, S.; Sun, X.; Yue, L.; Montgomery, S. M.; Demoly, F.; Zhou, K.; Zhao, R. R.; Qi, H. J. 4D Printing of Freestanding Liquid Crystal Elastomers via Hybrid Additive Manufacturing. *Adv. Mater.* **2022**, *34*, 2204890.
(45) López-Valdeolivas, M.; Liu, D.; Broer, D. J.; Sánchez-Somolinos, C. 4D Printed Actuators with Soft-Robotic Functions. *Macromol. Rapid Commun.* **2018**, *39*, 1700710.
(46) Wang, Z.; Wang, Z.; Zheng, Y.; He, Q.; Wang, Y.; Cai, S. Three-Dimensional Printing of Functionally Graded Liquid Crystal Elastomer. *Sci. Adv.* **2020**, *6*, No. eabc0034.
(47) Li, G.; Wong, T.-W.; Shih, B.; Guo, C.; Wang, L.; Liu, J.; Wang, T.; Liu, X.; Yan, J.; Wu, B.; Yu, F.; Chen, Y.; Liang, Y.; Xue, Y.; Wang, C.; He, S.; Wen, L.; Tolley, M. T.; Zhang, A.-M.; Laschi, C.; Li, T. Bioinspired Soft Robots for Deep-Sea Exploration. *Nat. Commun.* **2023**, *14*, 7097.
(48) Wang, T.; Joo, H.-J.; Song, S.; Hu, W.; Keplinger, C.; Sitti, M. A Versatile Jellyfish-like Robotic Platform for Effective Underwater Propulsion and Manipulation. *Sci. Adv.* **2023**, *9*, No. eadg0292.
(49) Byun, J.; Park, M.; Baek, S.-M.; Yoon, J.; Kim, W.; Lee, B.; Hong, Y.; Cho, K.-J. Underwater Maneuvering of Robotic Sheets through Buoyancy-Mediated Active Flutter. *Sci. Robot.* **2021**, *6*, No. eabe0637.
(50) Pratten, N. A. The Precise Measurement of the Density of Small Samples. *J. Mater. Sci.* **1981**, *16*, 1737−1747.

https://doi.org/10.1021/acsami.5c08610
ACS Appl. Mater. Interfaces 2025, 17, 47456−47465

Supporting Information

Multimodal Locomotion of Amphibious Soft Microrobots for Multi-Environment Exploration

Chenglin Li, Jing Li, and Xin Yi*
School of Mechanics and Engineering Science, Peking University, Beijing 100871, China
*Email: xyi@pku.edu.cn (X.Y.)

The file includes:

Supplementary text
Figures S1 to S27
Table S1
Legends for Movies S1 to S11

Other Supplementary Materials for this work include the following:

Movies S1 to S11

■ SUPPLEMENTARY TEXT

Materials. The liquid crystal monomers 1,4-bis-[4-(3-acryloyloxypropyloxy)benzoyloxy]-2-methylbenzene (RM257) and 1,4-bis-[4-(6-acryloyloxy-hexyloxy)benzoyloxy]-2-methylbenzene (RM82) were obtained from Shanghai Bide Pharmatech Co., Ltd. and Tianjin Hiens Optech Co., Ltd., respectively. The chain extender 2,2-(ethylenedioxy)diethanethiol (EDDET) was sourced from Shanghai Dibao Biotechnology Co., Ltd. The vinyl crosslinker 1,3,5-triallyl-1,3,5-triazine-2,4,6(1H,3H,5H)-trione (TATATO) and the antioxidant butylated hydroxytoluene (BHT) were purchased from Beijing Bailing Wei Technology Co., Ltd. The photoinitiator Irgacure 819 was acquired from BASF, and the catalyst dipropylamine (DPA) was obtained from TCI. Acetone, used as a solvent, was supplied by Beijing Tongguang Fine Chemical Co., Ltd. Ecoflex 0050 was procured from Smooth-On Inc., and ethanol (99.5%) was provided by Sinopharm Chemical Reagent Beijing Co., Ltd.

4D Printing of LCE. The 4D-printed LCE structures were fabricated using a custom-built Direct Ink Writing (DIW) printing system, as illustrated in Figure S4. The system comprises an air compressor (ATEC Shantron Silent Oil-free Air Compressor AT60/25, China), an air pressure controller (Bangyuan, China), a black syringe barrel, a 365 nm ultraviolet (UV) light source, and a three-axis displacement stage. The printhead, with an inner diameter of 0.6 mm, was used to extrude the LCE ink under controlled air pressure, ensuring sufficient shear force for precise alignment of the liquid crystal (LC) mesogens. During the DIW process, the printing speed was adjusted according to the extrusion pressure, and the temperature was maintained at room temperature. The extruded LCE ink was immediately exposed to UV light (~2 mW cm^{-2}) for partial curing. After printing, the top and bottom surfaces of the LCE samples were further cured under UV light (~30 mW cm^{-2}) for 15 minutes each to ensure complete crosslinking and facilitate detachment from the substrate. The printing models were designed using SolidWorks 2020 software, and the printing parameters were controlled by modifying the G-code in Simplify3D.

Measurement of Buoyancy Disks Buoyancy Variations. To measure real-time buoyancy changes in the buoyancy disk, we employed the hydrostatic weighing method, a well-established technique for quantifying buoyant forces (ref. 50). A custom test system was constructed, consisting of the buoyancy disk, electronic scales, a power supply, and a 50 g reference weight (Figure S20A). The buoyancy disk was fully immersed in deionized water at 23°C, and a 50 μm copper wire was used to deliver electrical power. When the power supply was activated, the hydrostatic weight of the buoyancy disk changed as a function time t according to the following equations

$$\frac{\Delta\rho(t)}{\rho} = -\frac{\Delta V(t)}{V} = -\frac{\Delta m(t)}{\rho_{\text{liq}} V}, \tag{1}$$

$$\Delta m(t) = \Delta\rho(t) \times \Delta V(t), \tag{2}$$

where $\Delta m(t)$, $\Delta\rho(t)$, and $\Delta V(t)$ represent the time-dependent variations in weight, density, and volume of the buoyancy disk after its underwater activation. ρ_{liq} represents the density of deionized water. Using these equations, we calculated the variations in buoyant force $\Delta F_b(t)$ and disk density $\Delta\rho(t)$. Heating for 60 s and cooling for 30 s under input currents ranging from 0.3 A to 0.5 A, we measured the time-dependent changes in buoyancy and density. The corresponding curves are presented in Figure S20.

Underwater Swimming Experiment Setup. The swimming experiments were conducted in a water tank with dimensions of 45 cm × 28 cm × 30 cm, filled with deionized water (Figure S23). Insulated copper wires (diameter: 50 μm) were connected to the buoyancy disk of the amphibious soft microrobot. To minimize the influence of the copper wires on the robot's swimming performance, buoyancy foam material was used to counterbalance their density. The robot's underwater motion was recorded using a video camera, and the resulting footage was analyzed for swimming behavior using Tracker software.

Swimming Control Strategy. To enable underwater swimming of the amphibious soft microrobot, we designed a buoyancy disk integrated with a flexible heating circuit B (Figure S3B$_2$). The heating circuit featured three independent fan-shaped heating regions, allowing precise control of buoyancy through Joule heating-induced density adjustments in the corresponding fan-shaped LFE regions. The total thickness of the buoyancy disk was 3 mm.

When only one fan-shaped heating region was activated, the generated buoyancy was insufficient to propel the microrobot underwater. To address this, we utilized a combination of coupled pairs from the three heating regions, which provided the directional momentum necessary for controlled underwater swimming. This approach enabled the microrobot to perform multidirectional swimming motions. When all three heating regions were activated simultaneously, the robot exhibited vertical upward swimming behavior. By combining these individual swimming behaviors, more complex motion patterns could be achieved.

To facilitate precise control of the heating regions, a simple control circuit was designed, consisting of a power supply, a programmable logic controller, and an Arduino microcontroller (Figure S25).

Characterization. The thermal decomposition of the printed LCE samples was evaluated using a Thermogravimetric Analyzer (TGA, Mettler Toledo TGA/DSC 3+) under a nitrogen atmosphere. The temperature was ramped from 20°C to 600°C at a heating rate of 10°C/min. The nematic-isotropic transition temperature T_{NI} of the LCE inks was determined using a Differential Scanning Calorimeter (DSC Q200, TA Instruments, USA). Uncrosslinked LCE inks were sealed in TZero aluminum pans and subjected to a heating-cooling-heating cycle from –50°C to 150°C at a constant rate of 10°C/min. The samples were first heated to 100°C to erase thermal history, followed by isothermal holds at –50°C and 150°C for 1 minute each. Data from the heating ramps were analyzed to determine the glass transition temperature T_g and T_{NI} of the LCE inks.

The rheological properties of the inks were characterized using a controlled stress rheometer (Discovery HR-2 Hybrid Rheometer, TA Instruments) equipped with a 20 mm Peltier plate geometry and a 500 μm gap. Prior to each test, the LCE inks were heated to 100°C to eliminate structural history and then equilibrated at the measurement temperature for 300 s. Viscosity measurements were performed by sweeping the shear rate from 0.01 s^{-1} to 1000 s^{-1}. Oscillatory measurements were conducted to determine the storage and loss moduli by applying stress sweeps from 0.01 Pa to 1 kPa at a frequency of 1 Hz.

LCE actuation experiments were conducted using a hot plate, with samples heated from 25°C to 120°C at a rate of approximately 24°C/min. Actuation behavior was recorded using a digital camera and analyzed using ImageJ software.

The motion of the amphibious soft microrobot was recorded using a smartphone and a video camera (Pocket 3, DJI), and trajectories were analyzed using Tracker software. The microrobot was powered by a precision adjustable power supply (SS-305, A-BF). Temperature changes during actuation were monitored using an infrared thermographic camera (K20, HIKMICRO), while the temperature rise of the flexible heating circuit was measured with a contact thermocouple thermometer (UT325, UNI-T). The water temperature during underwater actuation experiments was maintained at 22°C. The buoyancy and density of the buoyancy disk were measured using an experimental analytical balance (NX-5003i, FAYA).

Programmable Spatial Motion of LCE. We printed spatially programmable LCE using a custom-built 3D printer with a nozzle diameter of 0.6 mm, a printing speed of 12 mm/s, and a layer thickness of 0.96 mm. This setup enabled reversible transformations of complex shapes. Figure S13A shows a 4D-printed rectangle measuring 60 mm in length and 9 mm in width, printed at a 180° orientation. When heated to 120°C, the LCE contracted along the printing direction, resulting in a lengthwise shrinkage of approximately 39%. Figure S13B illustrates a 4D-printed LCE square grid with a side length of 50 mm, printed at a 90° orientation. As the temperature increased to 120°C, the grid curled into a barrel shape. Figure S13C and S13D depicts rectangles (60 mm in length, 9 mm in width) and circles (25 mm in diameter) printed with alternating directions of 45° and –45°. Heating induced incompatible strains, causing out-of-plane deformations. At 120°C, the liquid crystals contracted in the alignment direction at the microscopic level, leading to tubular and saddle-shaped configurations for the rectangles and circles, respectively, at the macroscopic level. Figure S13E shows a circle with a diameter of 25 mm, printed with a helical path. As the temperature increased, the print paths of the LCE compressed against each other, causing the center of the circle to bulge. When the temperature reached 120°C, a cone shape was formed.

Force Analysis. The amphibious soft microrobot was modeled as two simplified components: a red part and a blue part, with the front and rear contact points denoted as foot A and foot B, respectively. The centers of mass of the red and blue parts were used as reference points for analysis. It was assumed that the microrobot maintained an ideal state during motion, with foot A as the origin and the positive x-axis aligned with the direction of motion (Figure S17). The

motion process was divided into three stages: Stage 1 (heating), Stage 2 (contraction), and Stage 3 (extension). A force analysis was conducted for each stage.

Stage 1: When power was applied, the blue part was uniformly heated above the nematic-isotropic transition temperature T_{NI}, initiating a driving tendency.

Stage 2: The bending actuation of the blue LCE amphibious actuator caused the red part to move forward, triggering a friction competition between foot A and foot B (denoted as f_{2A} and f_{2B}). Due to the asymmetry in the shapes of the red and blue parts, the contact area between foot A and the ground differed from that of foot B, causing most of the robot to lift. As a result, f_{2A} reached the sliding friction condition earlier than f_{2B}, causing foot A to slide to the right while foot B remained stationary.

The kinematic equations for the red parts are

$$\begin{cases} m_{\mathrm{R}}\ddot{x}_{2\mathrm{R}} = F_{2\mathrm{R}}\cos a_2 - f_{2\mathrm{A}} - F_{2\mathrm{B}}\cos\beta_2, \\ m_{\mathrm{R}}\ddot{y}_{2\mathrm{R}} = T_{2\mathrm{R}} + F_{2\mathrm{R}}\sin a_2 + F_{2\mathrm{B}}\sin\beta_2 - G_{2\mathrm{R}}, \end{cases} \tag{3}$$

and the kinematic equations for the blue parts are

$$\begin{cases} m_{\mathrm{B}}\ddot{x}_{2\mathrm{B}} = F_{2\mathrm{R}}\cos a_2 + f_{2\mathrm{B}} - F_{2\mathrm{B}}\cos\beta_2\,, \\ m_{\mathrm{B}}\ddot{y}_{2\mathrm{B}} = T_{2\mathrm{B}} + F_{2\mathrm{B}}\sin\beta_2 + F_{2\mathrm{R}}\sin a_2 - G_{2\mathrm{B}}. \end{cases} \tag{4}$$

Stage 3: When power was turned off, the blue part cooled below T_{NI} and began to recover its original shape. The extension of the asymmetrical shapes of the red and blue parts reversed the directions of the friction forces (f_{3A} and f_{3B}), initiating a new cycle of friction competition. In this stage, f_{3B} reached the sliding friction threshold first, causing foot B to slide to the right while foot A remained stationary until the robot returned to Stage 1.

The kinematic equations for the red parts are

$$\begin{cases} m_{\mathrm{R}}\ddot{x}_{3\mathrm{R}} = -F_{3\mathrm{R}}\cos a_3 + f_{3\mathrm{A}} + F_{3\mathrm{B}}\cos\beta_3, \\ m_{\mathrm{R}}\ddot{y}_{3\mathrm{R}} = T_{3\mathrm{R}} - F_{3\mathrm{B}}\sin\beta_3 - F_{3\mathrm{R}}\sin a_3 - G_{3\mathrm{R}}, \end{cases} \tag{5}$$

and for the blue parts are

$$\begin{cases} m_{\mathrm{B}}\ddot{x}_{3\mathrm{B}} = -F_{3\mathrm{R}}\cos a_3 - f_{3\mathrm{B}} + F_{3\mathrm{B}}\cos\beta_3\,, \\ m_{\mathrm{B}}\ddot{y}_{3\mathrm{B}} = T_{3\mathrm{B}} - F_{3\mathrm{R}}\sin a_3 - F_{3\mathrm{B}}\sin\beta_3 - G_{3\mathrm{B}}. \end{cases} \tag{6}$$

In Eqs. (3)-(6), m_{R} and G_{R} (m_{B} and G_{B}) represent the mass and gravity of the red (blue) part, respectively, while $x_{i\mathrm{R}}$ and $y_{i\mathrm{R}}$ ($x_{i\mathrm{B}}$ and $y_{i\mathrm{B}}$) denote the displacements of the centroids of the red (blue) part in the x- and y- directions at each stage i (i = 1,2,3). $F_{i\mathrm{R}}$ and $F_{i\mathrm{B}}$ are the tensile forces exerted by one part on the other at each stage, while $T_{i\mathrm{R}}$ and $T_{i\mathrm{B}}$ represent the ground reaction forces of the red and blue parts. The angles α_i and β_i denote the inclinations of the red and blue parts relative to the ground at each stage. $f_{i\mathrm{A}}$ and $f_{i\mathrm{B}}$ represent the friction forces between foot A, foot B, and the ground.

The crawling motion of the microrobot in water was also analyzed. During this process, $F_{i\mathrm{Rb}}$ and $F_{i\mathrm{Bb}}$ denote the buoyancy forces acting on the red and blue parts at each stage. The governing equations are

In Stage 2: The kinematic equations for the red parts are

$$\begin{cases} m_{\mathrm{R}}\ddot{x}_{2\mathrm{R}} = F_{2\mathrm{R}}\cos a_2 - f_{2\mathrm{A}} - F_{2\mathrm{B}}\cos\beta_2\,, \\ m_{\mathrm{R}}\ddot{y}_{2\mathrm{R}} = T_{2\mathrm{R}} + F_{2\mathrm{Rb}} + F_{2\mathrm{R}}\sin a_2 + F_{2\mathrm{B}}\sin\beta_2 - G_{2\mathrm{R}}, \end{cases} \tag{7}$$

and for the blue parts are

$$\begin{cases} m_{\mathrm{B}}\ddot{x}_{2\mathrm{B}} = F_{2\mathrm{R}}\cos a_2 + f_{2\mathrm{B}} - F_{2\mathrm{B}}\cos\beta_2\,, \\ m_{\mathrm{B}}\ddot{y}_{2\mathrm{B}} = T_{2\mathrm{B}} + F_{2\mathrm{Bb}} + F_{2\mathrm{B}}\sin\beta_2 + F_{2\mathrm{R}}\sin a_2 - G_{2\mathrm{B}}. \end{cases} \tag{8}$$

In Stage 3: The kinematic equations for the red parts are

$$\begin{cases} m_{\mathrm{R}}\ddot{x}_{3\mathrm{R}} = -F_{3\mathrm{R}}\cos a_3 + f_{3\mathrm{A}} + F_{3\mathrm{B}}\cos\beta_3\,, \\ m_{R}\ddot{y}_{3\mathrm{R}} = T_{3\mathrm{R}} + F_{3\mathrm{Rb}} - F_{3\mathrm{B}}\sin\beta_3 - F_{3\mathrm{R}}\sin a_3 - G_{3\mathrm{R}}, \end{cases} \tag{9}$$

and for the blue parts are

$$\begin{cases} m_{\mathrm{B}}\ddot{x}_{3\mathrm{B}} = -F_{3\mathrm{R}}\cos a_3 - f_{3\mathrm{B}} + F_{3\mathrm{B}}\cos\beta_3\,, \\ m_{\mathrm{B}}\ddot{y}_{3\mathrm{B}} = T_{3\mathrm{B}} + F_{3\mathrm{Bb}} - F_{3\mathrm{R}}\sin a_3 - F_{3\mathrm{B}}\sin\beta_3 - G_{3\mathrm{B}}. \end{cases} \tag{10}$$

Buoyancy Analysis. Geometric parameters of the amphibious soft microrobot are illustrated in Figure S27A. The buoyancy disk had a diameter d of approximately 23 mm, while the overall diameter D of the microrobot was approximately 50 mm. By adjusting the non-uniform buoyancy distribution of the buoyancy disk, precise control over the microrobot's movement direction was achieved. The buoyancy disk comprised three independent fan-shaped regions, each with a centroid (x_i,y_i) (i = 1,2,3) that generated independent buoyant forces F_i (i = 1,2,3) (Figure S27A). The components of the offset vector $\boldsymbol{\delta}$ between the buoyancy center and the centroid are

$$\delta_x = \frac{\sum \Delta F_i \times x_i}{\sum \Delta F_i}, \quad \delta_y = \frac{\sum \Delta F_i \times y_i}{\sum \Delta F_i}. \tag{11}$$

The non-uniform buoyancy distribution generated a driving torque τ through the buoyancy center offset δ, expressed as

$$\tau = \delta \Delta F_{\mathrm{b}} = \delta \rho_{\mathrm{f}} g \Delta V, \tag{12}$$

where ρ_{f}, g, and ΔV represent the fluid density, gravitational acceleration, and the volume change induced by the activation of the buoyancy disk, respectively.

The swimming direction of the microrobot was determined by the combined effect of the buoyancy center offset and the driving torque. When swimming toward the negative x-direction, the two fan-shaped regions of the buoyancy disk on the negative x-side of the buoyancy disk were activated. This caused the buoyancy center to shift leftward ($\delta_x < 0$), generating a clockwise torque (Figure S27B).

Table S1. Summary of Thermally Actuation-Based Soft Robots

Thermal responsive materials	Heaters	Locomotion performance	Refs.
LCE/Graphene	Graphene	Land crawling (multi-directional) & wall climbing	11
LCE/Silver nanowires (AgNWs)	AgNWs	Land crawling (multi-directional)	21
LCE/Cu	Cu wires	Land walking (multi-directional)	22
Gold nanorod (AuNR)/LCE	AuNR	Land crawling (unidirectional)	30
LCE/Ni-Cr wires	Ni-Cr wires	Land crawling (unidirectional)	31
LCE	Hot plate	Land crawling (unidirectional)	32
LCE/Carbon nanotubes (CNTs)	CNTs	Swimming (multi-directional)	34
LCE	Photo response	Swimming (unidirectional)	35
LCE/Liquid metal (LM)	LM	Land crawling (unidirectional)	36
LCE/Cr-Au mesh	Cr-Au mesh	Land crawling (multi-directional)	37
LCE/Thermoelectric device (TED)	TED	Land walking (multi-directional)	38
LCE/LM	LM	Land crawling (multi-directional)	43
LCE/Cu	Cu	Amphibious crawling & swimming (both multi-directional)	Present work

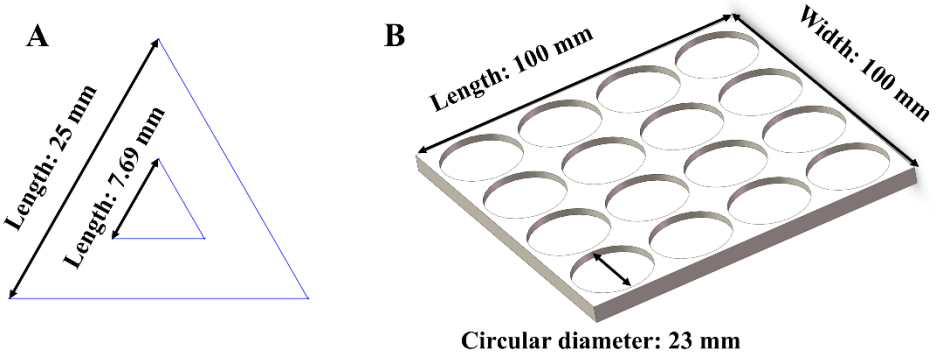

Figure S1. Amphibious soft microrobot structural design. (A) The glass fiber sheet structure. (B) The 3D-printed LFE manufacturing mold.

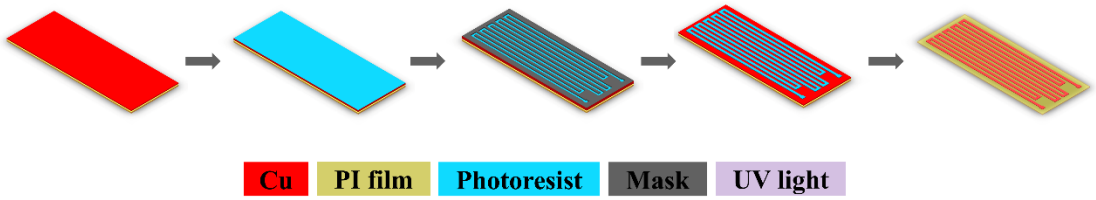

Figure S2. Schematic illustration of the preparation of flexible heated circuits using image reversal optical lithography and wet etching.

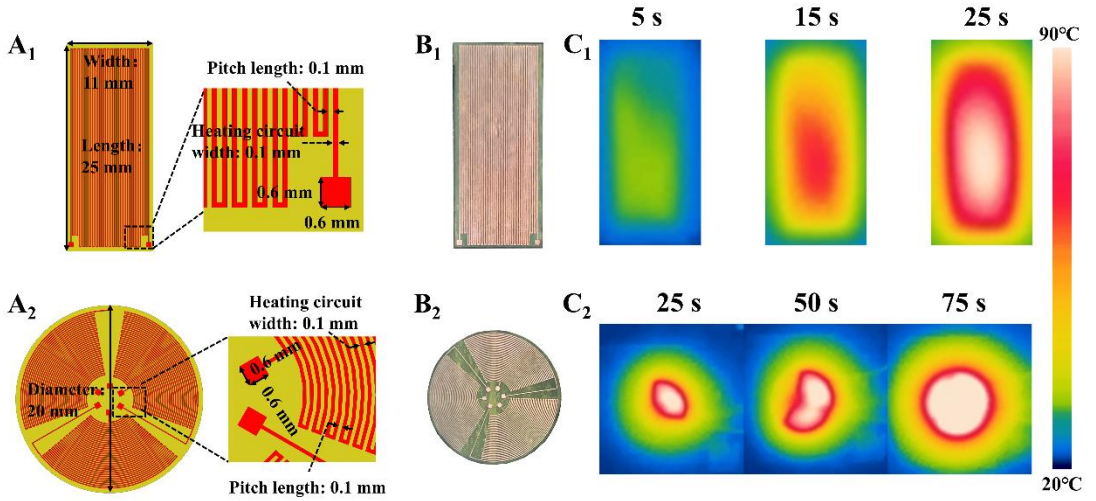

Figure S3. Flexible heating circuit structure and design. Geometry of the flexible heating circuits A (A_1) and B (A_2). Optical images of the heating circuits A (B_1) and B (B_2). Thermographic images of the heating circuits A (C_1) and B (C_2) after activation.

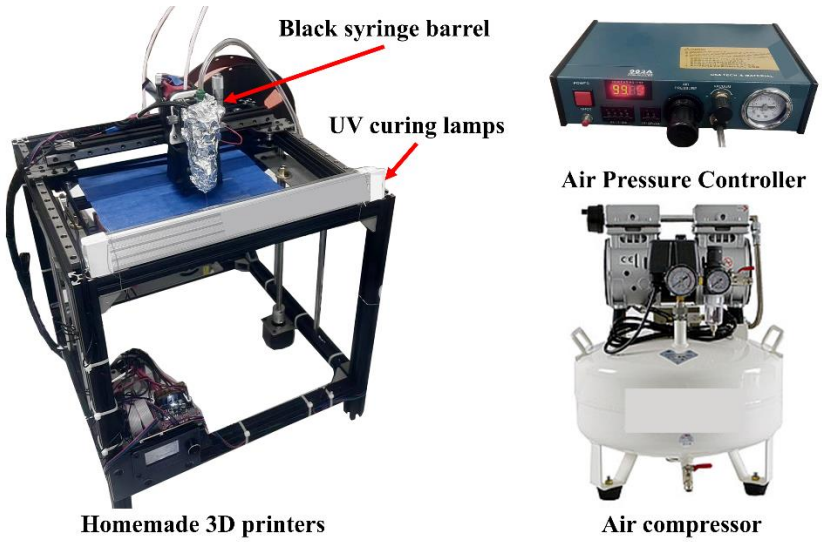

Figure S4. Diagram of the built DIW printing system.

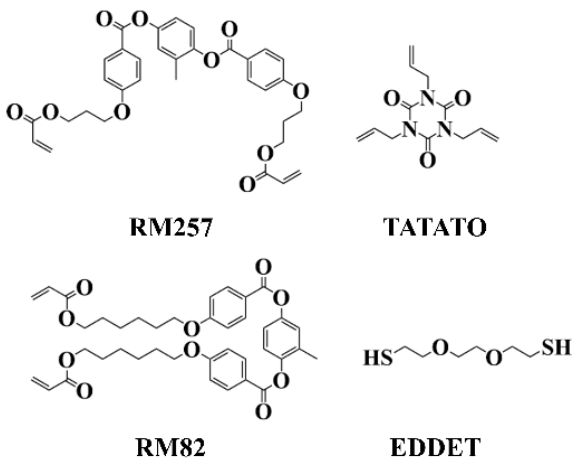

Figure S5. Main chemical components used in the preparation of LCE inks. 1,4-Bis-[4-(3-acryloyloxypropyloxy)benzoyloxy]-2-methylbenzene (RM257), 1,4-bis-[4-(6-acryloyloxy-hexyloxy)benzoyloxy]-2-methylbenzene (RM82), 1,3,5-triallyl-1,3,5-triazine2,4,6(1H,3H,5H) -trione (TATATO), and 2,2-(ethylenedioxy) diethanethiol (EDDET).

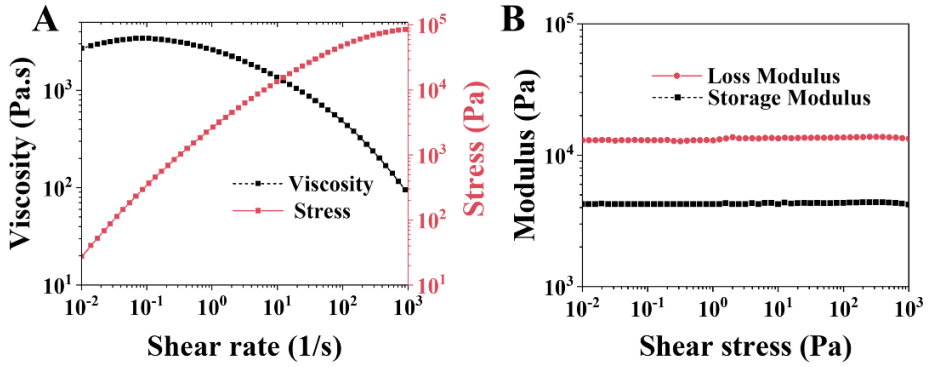

Figure S6. Rheological properties of the LCE inks at printing temperature of 25°C via the oscillatory measurement at 1 Hz. (A) Viscosity and shear stress as functions of shear rate for the LCE inks. (B) Storage modulus G′ and loss modulus G″ of the LCE inks versus shear stress.

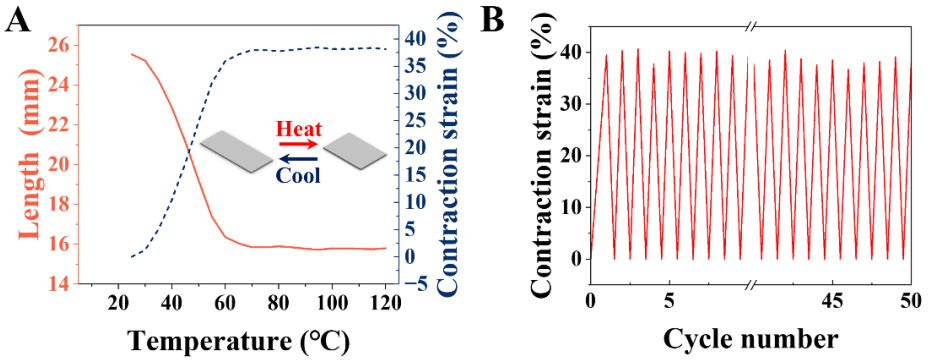

Figure S7. Contraction strain properties of the 4D-printed LCE samples. (A) Profiles of length and contraction strain of the LCE samples at different temperatures. (B) Contraction strain of the LCE samples recorded over multiple cycles, showing no malfunction and significant change.

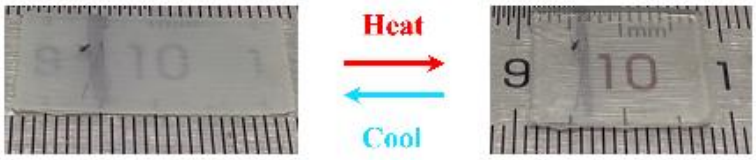

Figure S8. Optical images of the LCE samples before and after heat contraction.

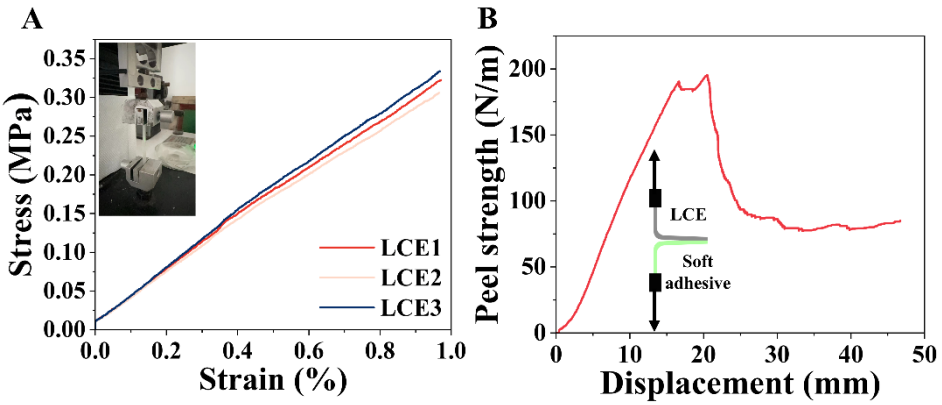

Figure S9. Mechanical and adhesive properties of LCE. (A) Engineering stress–strain curves of printed LCE samples at room temperature. (B) Peel strength of soft adhesive with an LCE sample.

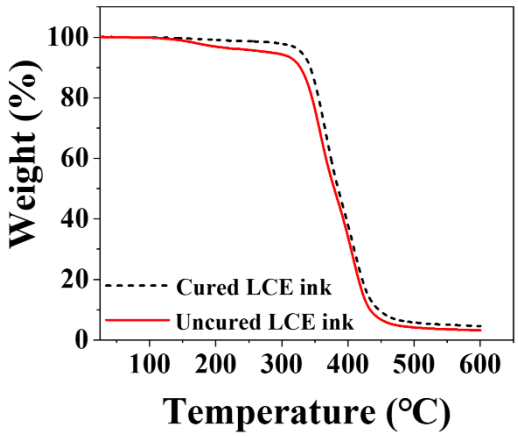

Figure S10. Thermogravimetric analysis of the LCE inks before and after curing.

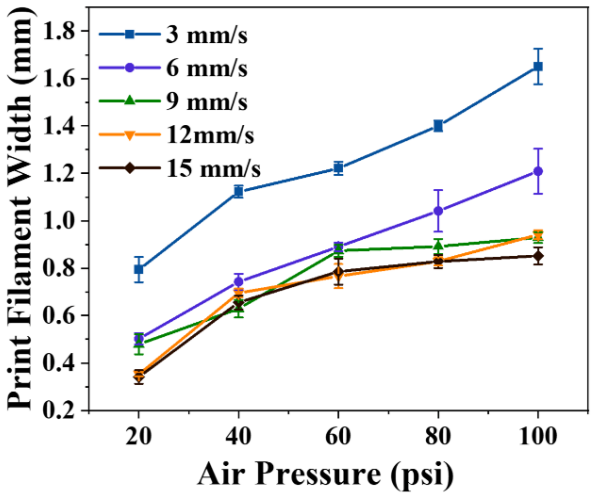

Figure S11. Variations in the widths of the LCE filaments at different printing speeds (3 mm/s to 15 mm/s) and air pressures (20 psi to 100 psi).

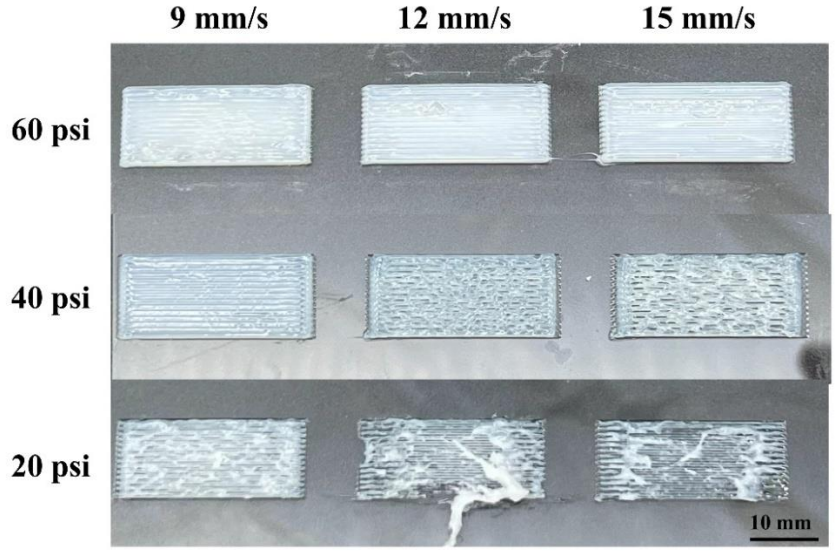

Figure S12. Optical images of LCE samples at different printing speeds and air pressures.

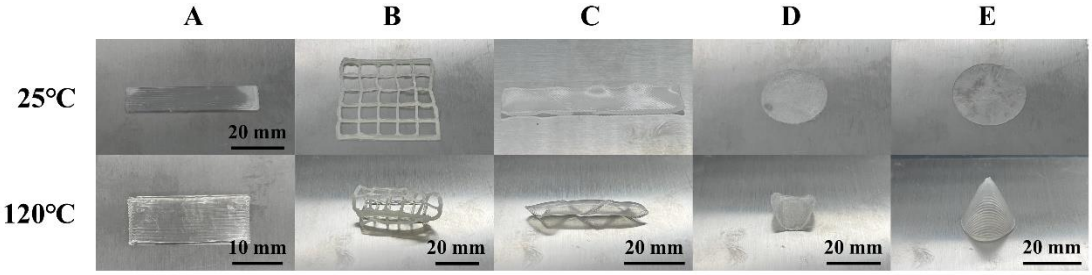

Figure S13. Programmable spatial motion of LCE samples via DIW printing. Rectangles (A) and grids (B) printed at angles of 180° and 90°, respectively. Rectangle (C) and circles (D) printed at angles of ±45°. (E) The sample with a spiral-shaped circular printing path.

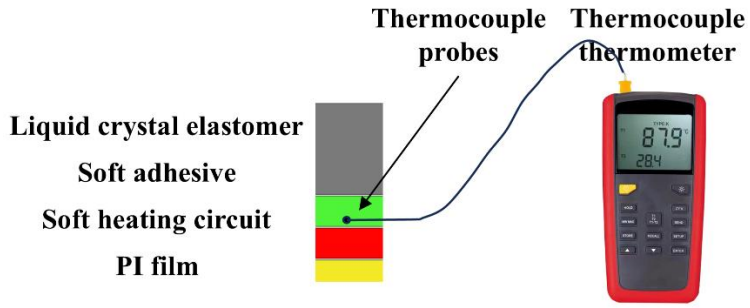

Figure S14. Schematic of internal temperature variation in the LCE amphibious actuator measured using a thermocouple thermometer.

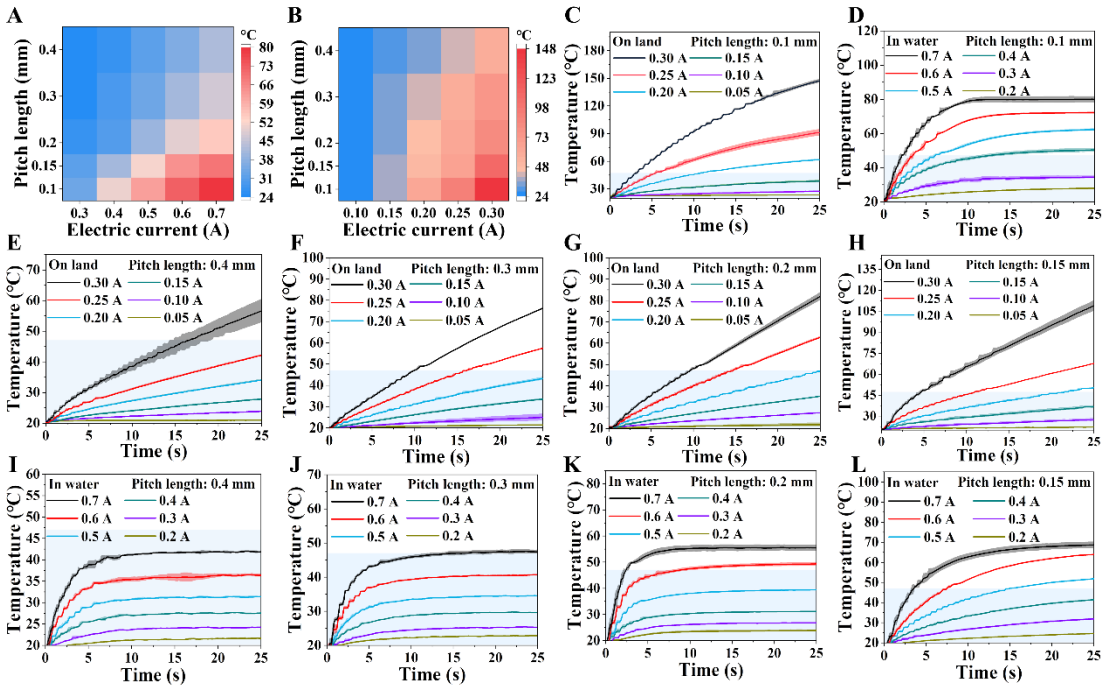

Figure S15. Heating performance of the LCE amphibious actuator driven by flexible heating circuit A. Thermal maps of Joule heating (°C) for the LCE amphibious actuator at different input currents, in water (A) and on land (B). Temperature-time curves of the LCE amphibious actuator with pitch lengths of 0.1 mm (C), 0.15 mm (H), 0.2 mm (G), 0.3 mm (F), and 0.4 mm (E) under Joule heating on land. Temperature-time curves of the LCE amphibious actuator with pitch lengths of 0.1 mm (D), 0.15 mm (L), 0.2 mm (K), 0.3 mm (J), and 0.4 mm (I) under Joule heating in water.

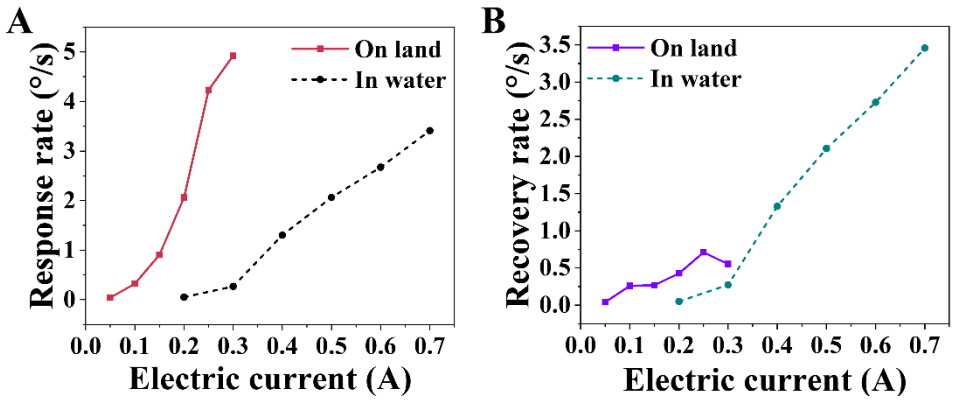

Figure S16. Response (A) and recovery rates (B) of the LCE amphibious actuators driven by different levels of input current.

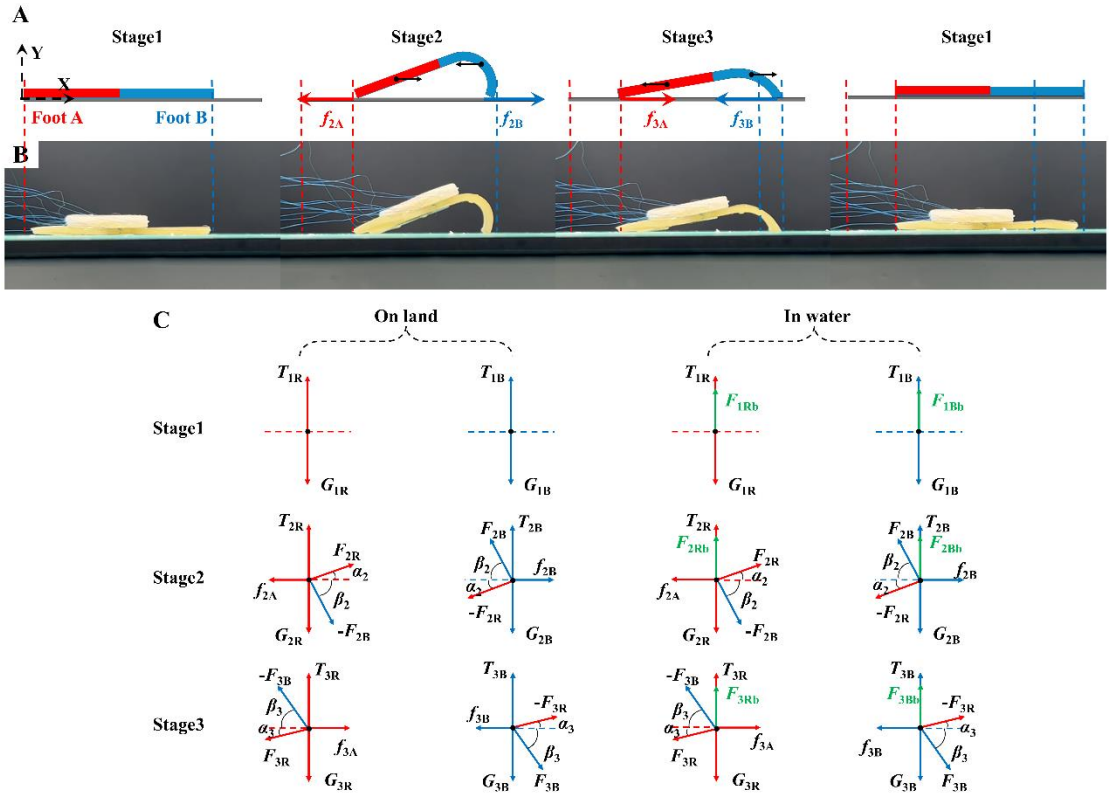

Figure S17. Force analysis of the amphibious soft microrobot. Schematic diagram (A) and physical image (B) illustrating the motion process during Stage 1 (heating), Stage 2 (contraction), and Stage 3 (extension). (C) Force analysis of the red and blue regions during the three stages.

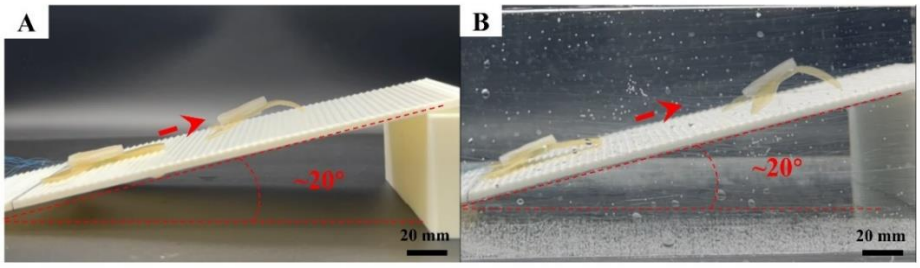

Figure S18. Climbing performance. Optical images of an amphibious soft microrobot crawling on a 20° inclined ratchet surface on land (A) and in water (B).

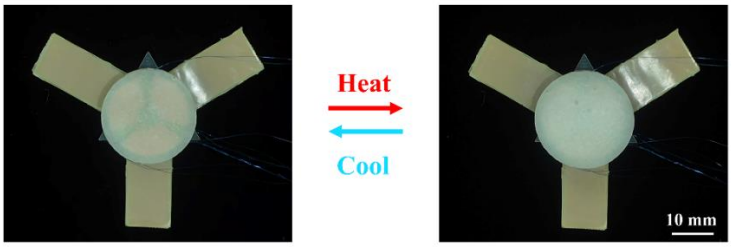

Figure S19. Optical images of the buoyancy disk before and after activation.

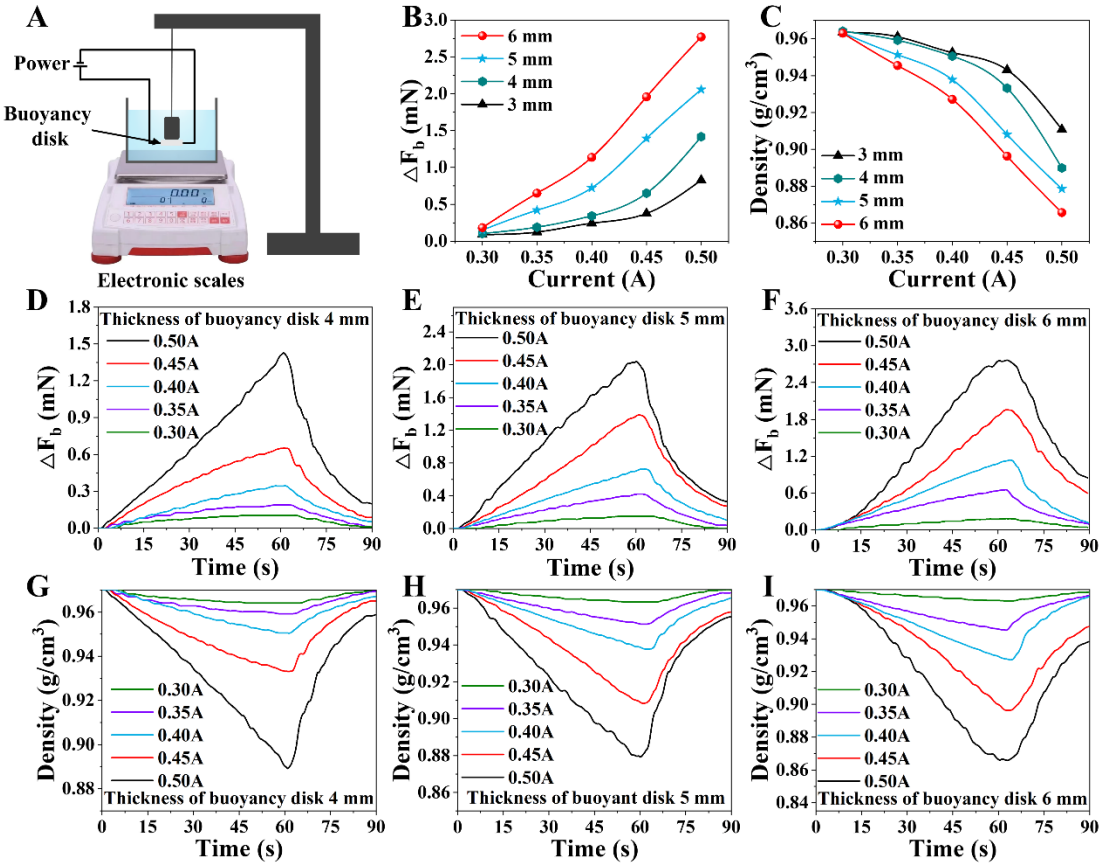

Figure S20. Characterization of buoyancy and density of the buoyancy disk. (A) Schematic diagram of the buoyancy test setup. Variation curves of buoyancy (B) and density (C) for the buoyancy disks of different thicknesses under varying input currents. Buoyancy variation curves (D-F) and density variation curves (G-I) for buoyancy disks at different thicknesses.

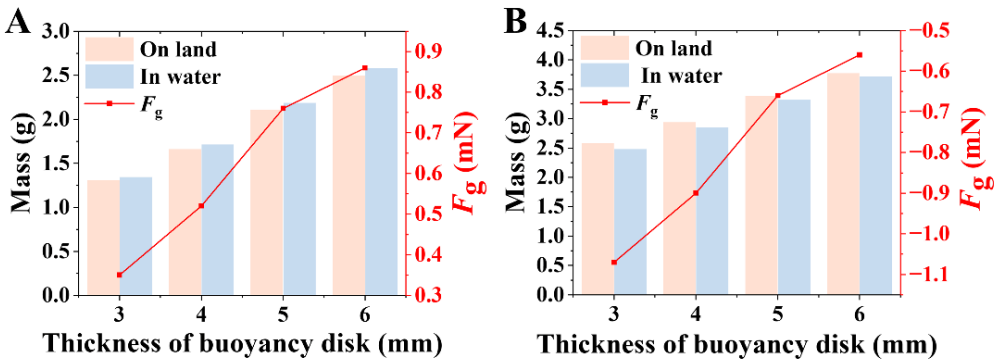

Figure S21. Characterization of initial resultant force F_g and mass as functions of the thickness values of the buoyancy disks (A) and the amphibious soft microrobot (B).

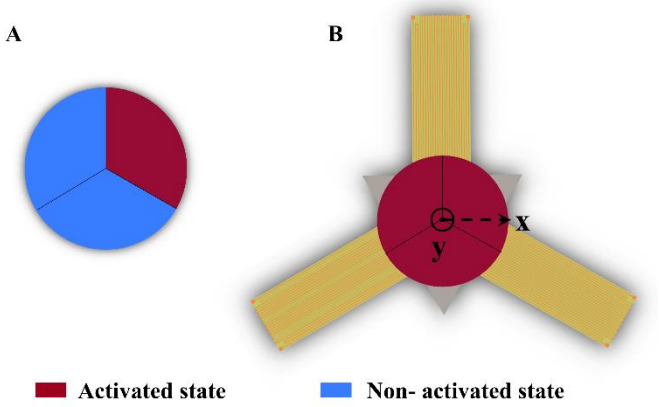

Figure S22. Characterization of the buoyancy disk in the amphibious soft microrobot. (A) Fan-shaped heating area of flexible heating circuit B during the buoyancy test. (B) Fan-shaped heating area of circuit B during the microrobot's vertical swimming (Figure 4I).

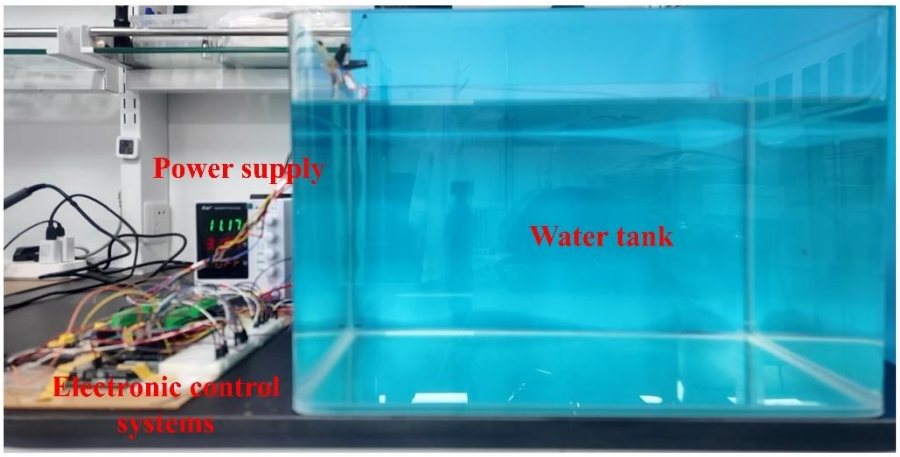

Figure S23. Experimental setup for underwater swimming tests of the amphibious soft microrobot.

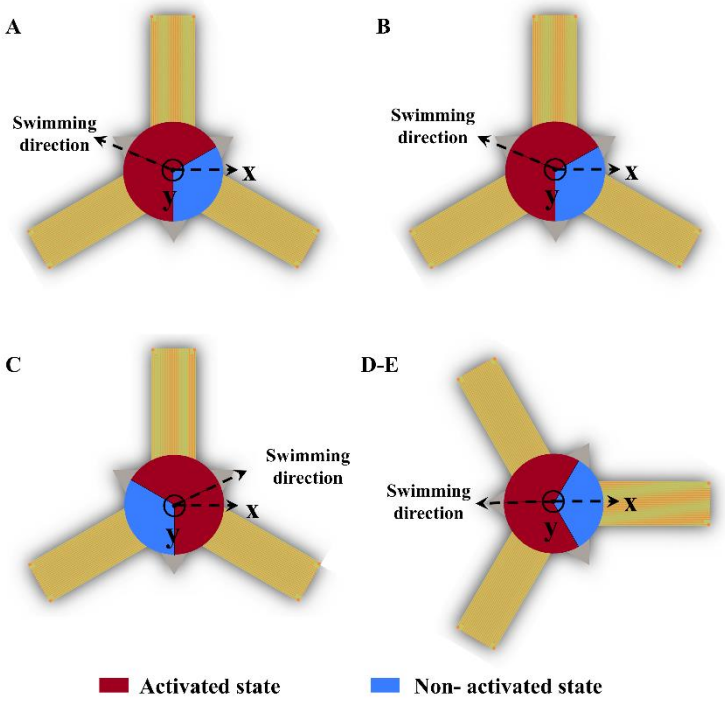

Figure S24. Fan-shaped heating regions of the buoyancy disk enabling underwater motion of the amphibious soft microrobot. (A) Hovering, (B) swimming in the negative *x*-direction, (C) swimming in the positive *x*-direction, (D) crossing an obstacle, and (E) passing through a narrow gap.

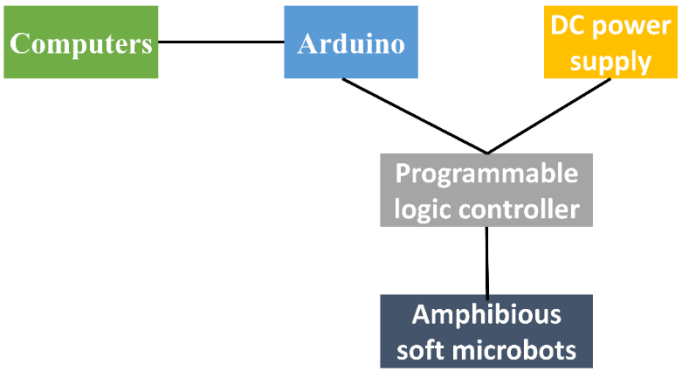

Figure S25. Schematic diagram of the drive system for the amphibious soft microrobot.

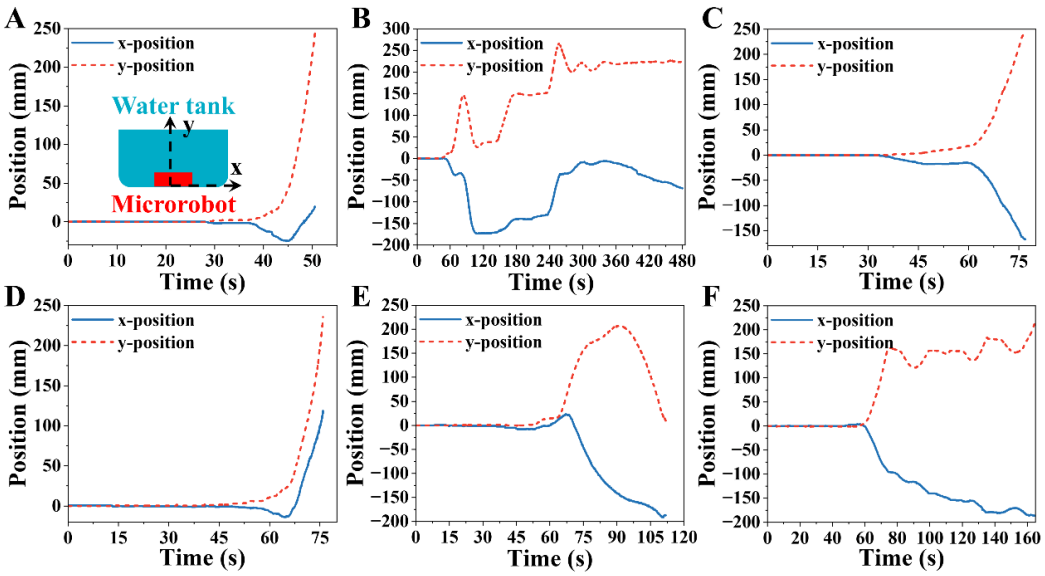

Figure S26. Position changes of the amphibious soft microrobot during underwater swimming in the *x*- and *y*- directions. (A) Vertical swimming, (B) hovering, (C) swimming in the negative *x*-direction, (D) swimming in the positive *x*-direction, (E) crossing an obstacle, and (F) passing through a narrow gap.

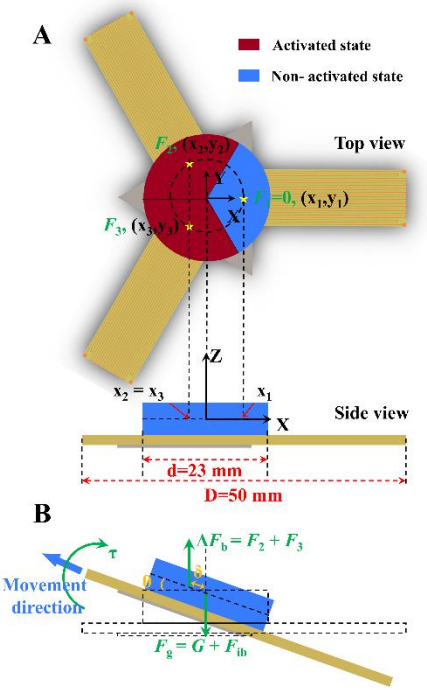

Figure S27. Directional swimming of an amphibious soft microrobot with non-uniform buoyancy distribution. (A) Non-uniform buoyancy distribution F_i (i = 1,2,3) and geometrical parameters of the microrobot. The mass center of the fan-shaped region i of the buoyancy disk is denoted denoted as (x_i,y_i) (i = 1,2,3). (B) Schematic diagram of the microrobot, showing the net upward momentum and torque generated by the offset of the center of ΔF_b from F_g (the difference between the robot's gravity and initial buoyancy).

Supplementary Movie Legends (Movies S1–S11):

Movie S1. Direct ink writing-based 4D printing of liquid crystal elastomer (LCE) ink.

Movie S2. Bending angle response of the LCE amphibious actuator to varying input currents on land and in water.

Movie S3. A crawling cycle of the amphibious soft microrobot.

Movie S4. Unidirectional and multi-directional crawling of the amphibious soft microrobot on land.

Movie S5. Unidirectional and multi-directional crawling of the amphibious soft microrobot in water.

Movie S6. Transition of the amphibious soft microrobot from land to water while carrying a 5.5 g payload, and climbing performance on land and in water.

Movie S7. Vertical swimming of the amphibious soft microrobot in water.

Movie S8. Hovering behavior of the amphibious soft microrobot at different water depths.

Movie S9. Swimming of the amphibious soft microrobot along *x*-direction in water.

Movie S10. The amphibious soft microrobot crossing an obstacle via swimming.

Movie S11. The amphibious soft microrobot navigating through a narrow gap underwater.